Rapid kinetic fingerprinting of single nucleic acid molecules by a FRET-based dynamic nanosensor

Kunal Khanna [a,2], Shankar Mandal [a,2], Aaron T. Blanchard [a,b,c], Muneesh Tewari [b,d,e,f], Alexander Johnson-Buck [a,d,e,**,1], Nils G. Walter [a,e,f,*]

[a] Single Molecule Analysis Group, Department of Chemistry, University of Michigan, Ann Arbor, MI, 48109, United States
[b] Department of Biomedical Engineering, University of Michigan, Ann Arbor, MI, 48109, United States
[c] Michigan Society of Fellows, University of Michigan, Ann Arbor, MI 48109, United States
[d] Department of Internal Medicine, Division of Hematology/Oncology, University of Michigan, Ann Arbor, MI, 48109, United States
[e] Center for RNA Biomedicine, University of Michigan, Ann Arbor, MI, 48109, United States
[f] Center for Computational Medicine and Bioinformatics, University of Michigan, Ann Arbor, MI, 48109, United States

ARTICLE INFO

ABSTRACT

Biofluid-derived cell-free nucleic acids such as microRNAs (miRNAs) and circulating tumor-derived DNAs (ctDNAs) have emerged as promising disease biomarkers. Conventional detection of these biomarkers by digital PCR and next generation sequencing, although highly sensitive, requires time-consuming extraction and amplification steps that also increase the risk of sample loss and cross-contamination. To achieve the direct, rapid, and amplification-free detection of miRNAs and ctDNAs with near-perfect specificity and single-molecule level sensitivity, we herein designed a single-molecule kinetic fingerprinting assay, termed intramolecular single-molecule recognition through equilibrium Poisson sampling (iSiMREPS). iSiMREPS exploits a dynamic DNA nanosensor comprising a surface anchor and a pair of fluorescent detection probes: one probe captures a target molecule onto the surface, while the other transiently interrogates the target to generate kinetic fingerprints by intramolecular single-molecule Förster resonance energy transfer (smFRET) that are recorded by single-molecule fluorescence microscopy and identify the target after kinetic filtering and data analysis. We optimize the sensor design, use formamide to further accelerate the fingerprinting kinetics, and maximize sensitivity by removing non-target-bound probes using toehold-mediated strand displacement to reduce background. We show that iSiMREPS can detect, in as little as 10 s, two distinct, promising cancer biomarkers—miR-141 and a common *EGFR* exon 19 deletion—reaching a limit of detection (LOD) of ~3 fM and a mutant allele fraction among excess wild-type as low as 1 in 1 million, or 0.0001%. We anticipate that iSiMREPS will find utility in research and clinical diagnostics based on its features of rapid detection, high specificity, sensitivity, and generalizability.

1. Introduction

Circulating cell-free nucleic acids (cfNAs) have emerged as promising diagnostic biomarkers for diseases such as cancer (Anfossi et al., 2018; Schwarzenbach et al., 2011). Among various cfNAs, microRNAs (miRNAs) are short non-coding RNAs with gene regulatory function and great potential as biomarkers due to high biofluid concentration and stability (Anfossi et al., 2018). Another important class of cfNAs comprises circulating, tumor-derived DNAs (ctDNAs), such as mutant copies of the epidermal growth factor receptor (*EGFR*) gene that are commonly found in the blood of some patients with non-small cell lung cancer (NSCLC) (Gazdar, 2009). Detecting abnormal levels of these biomarkers in biofluids (e.g., blood, urine) via non-invasive liquid biopsies has been a major area of clinical interest (Crowley et al., 2013; Heitzer et al., 2015), thus necessitating cfNA detection approaches that are rapid, highly specific, ultrasensitive, and robust for analyzing diverse biomarkers.

Advanced techniques such as next generation sequencing (NGS) for

large-scale genome analysis (Schmitt et al., 2012) and digital PCR (Milbury et al., 2014) have arisen as gold standards for nucleic acid detection. Although they achieve high sensitivity for low abundance analytes and have sufficient specificity for allelic frequencies as low as 0.01% for ctDNA mutants, they require significant sample preparation, purification, enzymatic reactions, and amplification steps that are time-consuming and can introduce various errors and compromise assay performance when high specificity is necessary (Potapov and Ong, 2017). Several amplification-free methods (Cohen et al., 2017; Li et al., 2018; Wang and Zhang, 2015) for detecting cfNAs have been reported. However, the clinical utility of these techniques is constrained by upper limits on specificity imposed by the thermodynamics of nucleic acid binding (Zhang et al., 2012). Additionally, while a wide variety of innovative single molecule fluorescent based techniques (Akkilic et al., 2020; Ma et al., 2016) have been developed for ultrasensitive and rapid detection of nucleic acids utilizing non-enzymatic signal amplification steps, they suffer from lower specificity and dynamic range since many have a static readout that poorly distinguishes target-specific fluorescent signals from nonspecific background.

We recently reported an amplification-free single-molecule kinetic fingerprinting technique called Single Molecule Recognition through Equilibrium Poisson Sampling (SiMREPS) (Hayward et al., 2018; Johnson-Buck et al., 2015) for detection of miRNAs and ctDNAs from biofluids. SiMREPS uses single-molecule fluorescence microscopy to record the transient binding and dissociation of fluorescent probes to a surface-captured nucleic acid. Continuous imaging for ~10 min reveals repeated binding to individual captured molecules, yielding a time-resolved "kinetic fingerprint" that can be used to distinguish a target molecule from non-target molecules and non-specific background (Hayward et al., 2018; Johnson-Buck et al., 2015). While SiMREPS permits ultrahigh specificity, its sensitivity and speed are limited by the long acquisition times required to observe multiple probe binding events to each target molecule. While increasing fluorescent probe concentration would accelerate binding kinetics and permit faster acquisition times, the increased fluorescent background from diffusing probes would result in severe degradation of signal-to-noise in the measurement, effectively placing an upper limit on the speed of acquisition.

To overcome all of these limitations, we here developed a novel single-molecule Förster resonance energy transfer (smFRET)-based accelerated kinetic fingerprinting approach termed intramolecular SiMREPS, or iSiMREPS (Fig. 1). iSiMREPS introduces a dynamic DNA nanoscale sensor comprising a surface-immobilized anchor stably hybridized to a pair of fluorescent capture and query probes. The nanoscale intramolecular arrangement of the sensor creates a high local concentration of fluorescent probes. Thus, transient intramolecular interactions within the sensor result in rapid transitions between high- and low-FRET states in the presence of the correct target molecule, while showing almost no high-FRET signal in the absence of the target or in the presence of spurious targets. (Fig. 1). These FRET transitions reveal a characteristic kinetic fingerprint of the analyte that reduces false positives dramatically compared to a static readout because the signal must satisfy intensity thresholds and exhibit a specific kinetic signature that passes kinetic filtering criteria (Fig. 1). The rate of the transitions between high- and low-FRET states can be modulated by modifying sensor components and assay conditions and can be further increased by modifications that reduce thermodynamic stability of the probe-target complex (e.g. minimizing complementary base pairs, modifying the lengths of the sensor strands to facilitate transitions between both states, increasing temperature, or adding denaturant). Additionally, sensitivity can be improved by removing non-target-bound fluorescent probes via toehold-mediated strand displacement (TMSD) from invading strands, which lowers background fluorescence. Optimized iSiMREPS shows high sensitivity and ultrahigh specificity for detecting both a miRNA and a ctDNA in just 10 s acquisition per field of view (FOV), a 60-fold improvement over conventional (intermolecular) SiMREPS measurements, paving the way for dramatically accelerated molecular diagnostics.
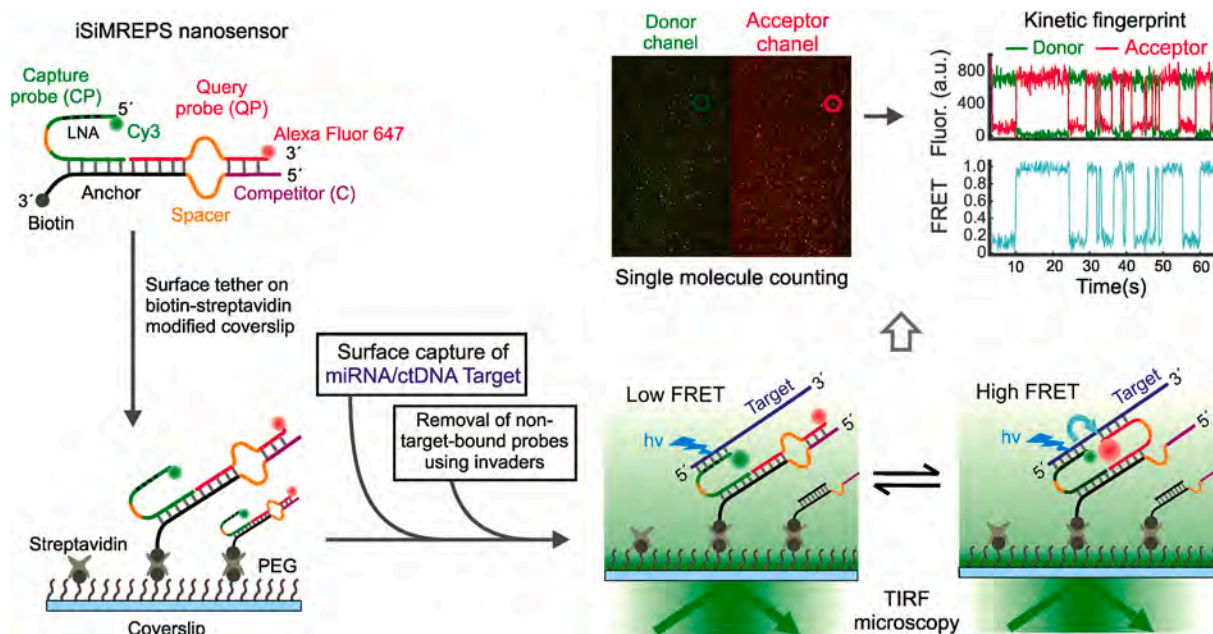
Fig. 1. Schematic of iSiMREPS sensor for rapid kinetic fingerprinting of single nucleic acids. The iSiMREPS nanosensor consists of a biotinylated, surface-tethered anchor hybridized to a capture probe (CP) and a query probe (QP). The CP is labeled with a donor fluorophore (Cy3) and partially modified with locked nucleic acid residues for high affinity capture of a miRNA/ctDNA target molecule. The QP contains an acceptor fluorophore (Alexa Fluor 647) and transiently alternates between binding target and competitor sequences to generate high- and low-FRET signals, respectively. Transitions between FRET states are recorded by total internal reflection fluorescence (TIRF) microscopy, and FRET vs. time traces are analyzed computationally to count single biomarker molecules with high specificity.

2. Material and methods

2.1. Oligonucleotides and reagents

All unmodified DNA oligonucleotides were purchased from Integrated DNA Technologies (IDT, www.idtdna.com) with standard desalting purification, unless otherwise noted. Biotinylated DNA oligonucleotides were purchased from IDT with polyacrylamide gel electrophoresis (PAGE) purification. Fluorescent query probes (QPs) with a 3′ Alexa Fluor 647 modification were purchased from IDT with high-performance liquid chromatography (HPLC) purification. Capture probes (CPs) that contained locked nucleic acid (LNA) residues were purchased either from IDT with a 5′Cy3 modification and HPLC purification or from Qiagen with a 5′amino modification with HPLC purification. The CPs from Qiagen were labeled with Cy3 monoreactive dye (GE Healthcare) and purified by ethanol precipitation (https://www.qiagen.com/us/resources). The miR-141 with a 5′-phosphate modification was purchased from IDT with HPLC purification. The double-stranded *EGFR* exon 19 deletion mutant DNA (*EGFR*$\Delta_{\text{exon\_19}}$) (COSMIC ID: COSM6223; c. 2235_2249del15 [p.E746_A750delELREA]) and wild type DNA (*EGFR*$_{\text{exon\_19}}$) substrates were prepared by annealing complementary single stranded oligonucleotides at 1 μM final concentration in annealing buffer (10 mM Tris-HCl, pH 8.0 at 25 °C, 50 mM NaCl and 1 mM EDTA), heating at 95 °C for 3 min, cooling to room temperature for 25 min, and finally holding at 4 °C for 10 min before storage at −20 °C for further use. All oligonucleotides' sequences are shown in Tables S1 and S2.

2.2. Design of iSiMREPS probes

The intramolecular SiMREPS sensor design requires a stable complex of the anchor, capture probe (CP), and query probe (QP) that does not dissociate from the imaging surface in iSiMREPS assay conditions. The anchor contained a 12-nt segment rich in GC content (≥75%) to have a melting temperature (T_m) of ~60 °C for stable hybridization with both CP and QP (Figs. 2A and 3A). The T_m between anchor and CP or QP was estimated by IDT OligoAnalyzer (https://www.idtdna.com/calc/analyzer) using the following parameters: target DNA concentration = 25 nM, NaCl = 600 mM, 25 °C. All iSiMREPS sensors contained identical sequences in the anchor to stably hybridize with CP and QP. The CPs contained an 11- to 12-nt target-capturing sequence with 4 LNA residues (T_m = ~70 °C, estimated using Qiagen web application) for high affinity and kinetically stable capturing of nucleic acid targets on the surface. All QPs used an 8-nt complementary segment for transient binding and dissociation with miR-141 (T_m = 30.2 °C) (Table S3) or *EGFR*$\Delta_{\text{exon\_19}}$ (T_m = 23.9 °C) (Table S4). The QPs also used a 6-7-nt complementary segment for transient binding with the competitor sequences extended from anchor for miR-141 (T_m = 7.5–18.1 °C) (Table S3) and a 6-8-nt complementary section for *EGFR*$\Delta_{\text{exon\_19}}$ (T_m = 0–23.9 °C) (Table S4). The T_m between query and target or competitor was estimated by IDT OligoAnalyzer as before, but with target RNA or DNA concentration = 1 μM. The discrimination between mutant (MUT) and wild-type (WT) DNA with a specific query probe was calculated using the web software NUPACK (Caltech:, 2007; Zadeh et al., 2011) and utilizing the following equation 1 (Zhang et al., 2012),

$$Q_{max,\ therm} = e^{-\Delta\Delta G^0/RT} \tag{1}$$

where $Q_{max,\ therm}$ is the maximum theoretical discrimination, $\Delta\Delta G^0$ is the difference in the Gibbs free energy of hybridization of a query with MUT and of the same query with WT DNA target. The detailed guidelines for designing SiMREPS query or fluorescent probes have been discussed elsewhere (Hayward et al., 2018; Johnson-Buck et al., 2015, 2019).

2.3. Objective-TIRF iSiMREPS assay design

Detection experiments using the objective-TIRF microscope used sample cells made of cut pipette tips that were attached to a biotin-PEG and mPEG passivated glass coverslip (see Supplementary Information (SI)). The sample cells were first treated with 45 μL of 0.1–0.5 mg/mL streptavidin in T50 (10 mM Tris-HCl pH 8.0, 50 mM NaCl) for 10–20 min. The subsequent steps for this assay followed one of two procedures.

One procedure, along with a prism-TIRF protocol (see SI), was followed for the initial optimization of iSiMREPS assay parameters and conditions for detecting miR-141. The anchor, capture, query strands and miR-141 target were combined at 200, 225, 250 and 5 nM final concentrations, respectively in 4 × PBS (Phosphate-buffered saline) (40 mM Na$_2$HPO$_4$, 7.2 mM KH$_2$PO$_4$, pH 7.4, 548 mM NaCl, 10.8 mM KCl), heated at 70 °C for 7 min in a metal bath, and then cooled at room temperature for 25 min. Unless otherwise noted, all nucleic acid samples preparation were performed in GeneMate low-adhesion 1.7 mL micro centrifuge tubes in 4 × PBS. The sensor was diluted 1000-fold, and 100 μL of the sensor solution was added to the cell for 45 min to tether the sensor on the surface via streptavidin-biotin affinity linkages. After removing non-surface-bound sensors and washing the cell 3 times with 4 × PBS, a 100 μL solution of a pair of invader strands (see Table S1), each at 2 μM, was added to the cell and incubated for 20 min to remove non-target-bound fluorescent probes from the imaging surface. Next, the invaders solution was removed, the cell was washed 3 times with 4 × PBS, and 180-200 μL imaging buffer containing oxygen scavenger system (OSS) consisting of 1 mM Trolox, 5 mM 3,4-dihydroxybenzoate, 50 nM protocatechuate dioxygenase, and the desired v/v% formamide in 4 × PBS was added in the cell which was then imaged by TIRF microscopy.

The other procedure was followed for all experiments for detecting *EGFR*$\Delta_{\text{exon\_19}}$ as well as miR-141 quantification. Unless otherwise noted, a synthetic forward strand of *EGFR*$\Delta_{\text{exon\_19}}$ was used for optimizing the sensor parameters and assay conditions, while all experiments for quantifying concentration and determining sensitivity and specificity used duplex *EGFR*$\Delta_{\text{exon\_19}}$. The anchor, capture, and query strands for miR-141 or *EGFR*$\Delta_{\text{exon\_19}}$ was combined in a PCR tube at 400–500 nM final concentrations in 4 × PBS, heated at 95 °C for 3 min, 72 °C for 7 min and 25 °C for 25 min and 4 °C for 10 min using a thermocycler to form a stable intramolecular complex. The sensor was then diluted to the desired concentration of 10 nM miR-141 sensor or 10–50 nM *EGFR*$\Delta_{\text{exon\_19}}$ sensor and 100 μL of the diluted sensor was added in the cell and incubated for 30 min to tether the sensor to the surface. Next, 100 μL of a solution containing either miR-141 or *EGFR*$\Delta_{\text{exon\_19}}$ target of the desired concentrations in 4 × PBS was applied in the cell for 90 min for efficient capturing of the target by surface-tethered sensors. *EGFR*$\Delta_{\text{exon\_19}}$ target solution containing 100 nM of auxiliary probe and 2 μM of dT$_{30}$ were heated at 90 °C for 3 min in a metal block and cooled in a water bath at room temperature for 3 min prior to cell application. The non-target-bound probes were removed by invaders before imaging under an objective-type TIRF microscope in presence of OSS as outlined above.

2.4. Single-molecule fluorescence microscopy

iSiMREPS experiments were performed using either an Olympus IX-71 prism-type TIRF microscope equipped with a 60 × water-immersion objective (Olympus UPLANAPO, 1.2 NA) or an Olympus IX-81 objective-type TIRF microscope equipped with a 60 × oil-immersion objective (APON 60XOTIRF, 1.49 NA) with CellTIRF and z-drift control modules. An ICCD (I-Pentamax, Princeton Instruments, MCP Gain 60) or sCMOS (Hamamatsu C13440–20CU) camera was used to record movies for the prism-TIRF while an EMCCD camera (IXon 897, Andor, EM gain 150) was used for the objective-TIRF. For recording smFRET signal, the Cy3-Alexa Fluor 647 fluorophore pairs were excited by light from a 532 nm laser at a power of 15–30 mW. For reliably detecting FRET signals with satisfactory S/N, an illumination intensity of ~50 W/cm^2 is typically

used, and the TIRF angle adjusted to achieve a calculated evanescent field penetration depth of ~70–85 nm. Two-channel images were recorded using a prism-TIRF microscope while only acceptor channel images were recorded using an objective-TIRF microscope. In prism-TIRF imaging, the signal integration time (exposure time) per frame was 100 ms, laser power was ~18 mW, and movies ranging from 1 to 15 min were collected to assess FRET behavior comprehensively. In objective-TIRF imaging, the exposure time per frame was 60–100 ms, and typically 200–600 movie frames were acquired per FOV.

2.5. Processing and analysis of objective-TIRF data

MATLAB scripts were used to identify areas of high average FRET acceptor intensity within each field of view, generate intensity-versus-time traces from these areas, and save these traces for further analysis. These traces were then analyzed using a two-state HMM (Bronson et al., 2009) algorithm to generate idealized (noise-less) intensity-versus-time traces to identify transitions between high- and low-FRET states. Thresholds of a minimum intensity of FRET transitions as well as a minimum S/N for the FRET signal were applied to each trace to distinguish genuine FRET transitions from baseline noise (Bronson et al., 2009) (Tables S6 and S7). Those traces passing the initial intensity and SNR thresholding were subjected to kinetic analysis to extract the number of FRET transitions per trace ($N_{b + d}$), the median dwell time in the high-FRET ($\tau_{on, median}$), and low-FRET states ($\tau_{off, median}$), the intensity of the low-FRET ($I_{low-FRET}$) and high-FRET ($I_{high-FRET}$) states, the longest individual dwell times in the high- and low-FRET states, and the coefficients of variation (CVs) of the dwell times in the high- and low-FRET states. These extracted parameters were subjected to minimum and maximum thresholding as indicated in Tables S6 and S7 to identify target-bound sensors based on their distinct kinetic and intensity behavior and to count the number of such target-bound sensors ("accepted counts") observed in each movie. In addition, the cumulative frequencies of the dwell times in the high- and low-FRET states were fit to a single or double exponential function (see SI, and Figs. S4, S8 and S9) to obtain the average dwell time in each state and generate $N_{b + d}$ histograms for each sensor. The $N_{b + d}$ histograms and average dwell times were used to evaluate the sensor's performance in terms of separation from background and capacity for rapid detection. The accepted counts were used for quantification and assessment of sensitivity. Prism-TIRF data was processed with similar considerations (See SI, and Table S5).

3. Results and discussion

3.1. The general architecture and working principles of smFRET-based iSiMREPS nanosensors for nucleic acids

smFRET-based iSiMREPS for counting single nucleic acid molecules utilizes a surface-immobilized nanoscale sensor composed of three DNA oligonucleotides: a biotinylated anchor, a donor (Cy3)-labeled capture probe (CP), and an acceptor (Alexa Fluor 647)-labeled query probe (QP) (Fig. 1). The anchor stably binds the non-labeled ends of the CP and QP. The free end of the CP is partially modified with locked nucleic acid (LNA) residues, enabling high-affinity capture of the miRNA/ctDNA target molecule. The free end of the QP is designed to alternate between transient hybridization to the free end of the captured target nucleic acid molecule and a competitor (C) sequence that extends from the free end of the anchor. We introduced poly-deoxythymidine (poly-dT) segments as spacers in the anchor, CP, and QP to introduce the flexibility necessary for the sensor to properly assemble and transition between target-bound and competitor-bound states.

In the optimized assay, iSiMREPS sensors composed of pre-hybridized anchor, CP, and QP are tethered first to a biotin-Bovine Serum Albumin (BSA)-passivated quartz slide (for prism-type total internal reflection fluorescence, or p-TIRF) or a PEG-passivated glass

coverslip (for objective-type TIRF or o-TIRF) via streptavidin-biotin affinity linkages. The nucleic acid target molecules are then introduced into the solution above the surface. The target molecule binds strongly to the CP and thus become tethered to the surface. To minimize background signals before TIRF imaging, non-target-bound fluorescent probes are removed from the surface by toehold mediated strand displacement (TMSD) using a pair of capture and query invader strands (see below for details).

In the presence of a target molecule, the QP alternates between transiently binding to the target and the competitor, yielding distinct FRET signatures depending on which sequence is bound. When the QP binds to the target, the donor and acceptor fluorophores are in close proximity, resulting in a high-FRET signal (Fig. 1). In contrast, when the QP dissociates from the target and/or binds to the competitor, the two fluorophores are far apart resulting in little to no FRET signal (Fig. 1). The repeated transitions between high- and low-FRET signals generate a characteristic kinetic fingerprint, permitting the accurate identification of single target nucleic acid molecules. Because these transitions occur much more rapidly than the transitions in conventional (intermolecular) SiMREPS, we anticipated that smFRET-based iSiMREPS should allow for faster and higher-confidence detection of nucleic acids through rapid fingerprint generation. In the following sections, we optimize this general design to detect two distinct nucleic acid biomarkers of disease.

3.2. Optimization of an iSiMREPS sensor design for detecting miRNA

An initial proof-of-concept iSiMREPS sensor (Fig. 2A) was designed to detect miR-141, a miRNA that has emerged as a biomarker for prostate cancer (Bryant et al., 2012; Mitchell et al., 2008). To develop iSiMREPS into an accelerated single-molecule kinetic fingerprinting technique, we initially tested several sensor designs (Figs. S1A–C) aiming for rapid smFRET transitions in the presence of target. To refer to different sensor designs, we use a $Q_a C_b QS_c CS_d$ naming convention, where Q is the query sequence complementary to target, QS is the query spacer, C is the competitor sequence complementary to the query sequence, CS is the competitor spacer, and the letters a, b, c, and d are integers reflecting the number of nucleotides in each domain (Fig. 2A).

We initially omitted a competitor sequence (CS_0) and instead used an 18-nt poly-dT query spacer (QS_{18}) to introduce conformational flexibility (Murphy et al., 2004) in the QP and generate high- and low-FRET signals (Fig. S1A). p-TIRF characterization of $Q_8 C_0 QS_{18} CS_0$ in the presence of miR-141 showed clear smFRET signals, suggesting that the sensor hybridized successfully with miR-141 to induce a high-FRET state (Fig. 2B). However, the equilibrium FRET distribution overwhelmingly favored the high-FRET state (Fig. 2B), preventing the characterization of a kinetic fingerprint. This bias likely occurred due to the desired high local effective concentrations (Li et al., 2016) of the probes resulting in a high rate of query and target association. Consequently, while query-target dissociation events are expected, they appear too short-lived to be detected at the 60–100 ms time resolution achievable in smFRET. To disfavor the query-target interaction by increasing the entropic cost of hybridization, we increased the length of the query spacer from dT_{18} to dT_{33} (Fig. S1A). However, $Q_8 C_0 QS_{33} CS_0$ still heavily favored the high-FRET state (Fig. S1D).

We hypothesized that the addition of a competitor sequence could decrease the observed dwell times of the target bound (high-FRET) state by competing with the target and stabilizing the non-target-bound (low-FRET) state (Fig. 1). Therefore, in next design we introduced a 7-nt competitor sequence (C_7) ($T_m = 18.1$ °C Table S3) to the anchor and used a 3-nt poly-dT as a competitor spacer (CS_3) (Fig. S1B). $Q_8 C_7 QS_{18} CS_3$ showed repeated transitions between high- and low-FRET states that constituted a distinctive kinetic fingerprint in the presence of miR-141 (Fig. 2C). In fact, this design was somewhat biased towards the low-FRET state. This experiment demonstrated that the competitor sequence is required for iSiMREPS designs to exhibit measurable transitions between smFRET states.
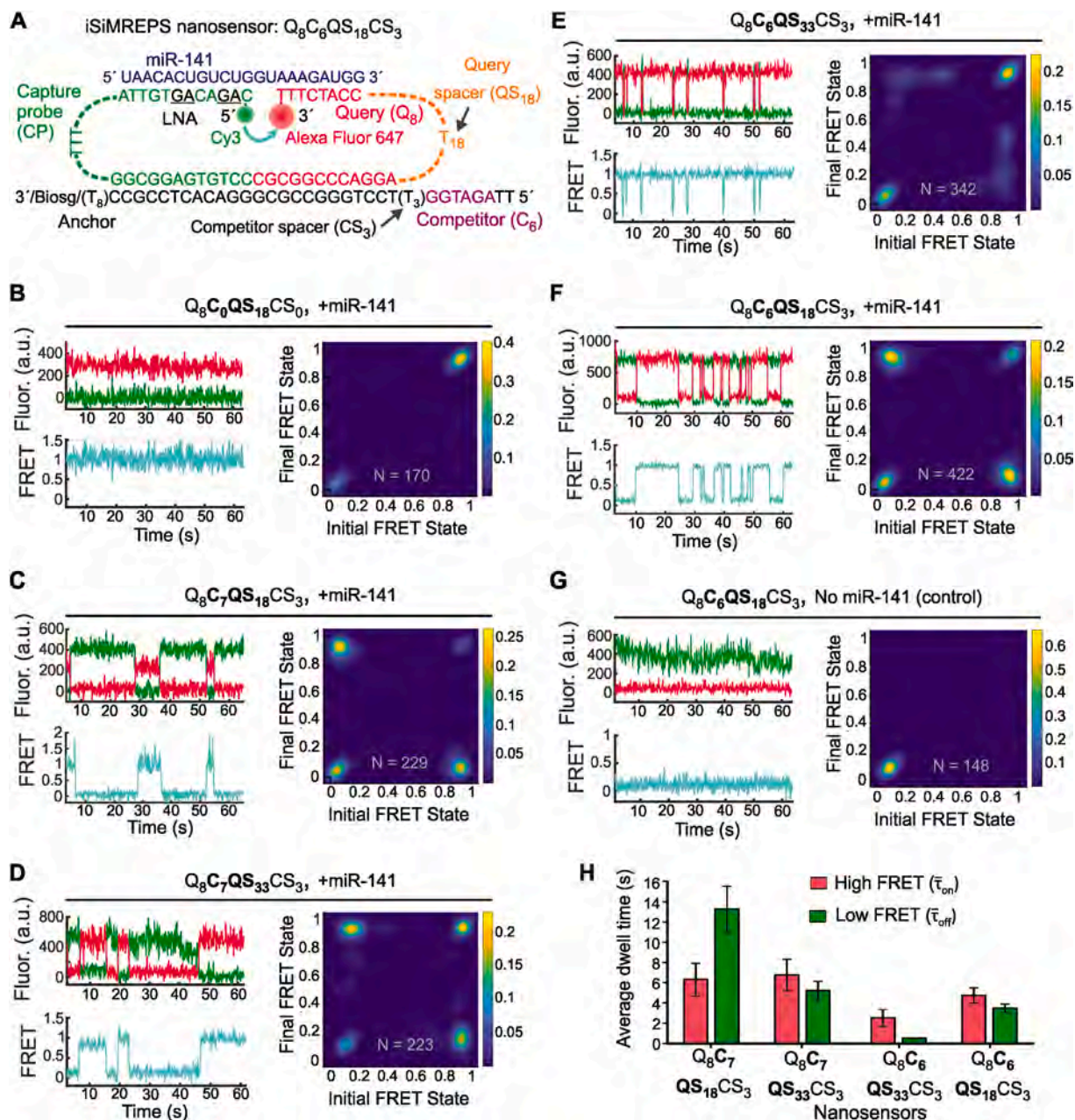
Fig. 2. Design and optimization of iSiMREPS for detection of a miRNA. (**A**) Design of the optimized $Q_8C_6QS_{18}CS_3$ smFRET-based iSiMREPS sensor for detection of miR-141. The CP stably binds with the miRNA target with the assistance of locked nucleic acid residues (black and underlined) that increase the stability of the DNA-RNA duplex. The query (8 nt) switches between being bound to the 8 nt overhang of the target or to a 6 nt competitor sequence that extends from the anchor, resulting in dynamic kinetic smFRET fingerprints. (**B-G**) TODP plots and representative traces for different iSiMREPS sensor designs that have fixed query (8 nt), varying competitor (6 and 7 nt), fixed competitor spacer (3 nt), and varying query spacer (3, 18 and 33 nt) lengths in the presence of miR-141, as well as control without miR-141. The smFRET dynamics of each sensor is indicated. (**H**) The average dwell times of the high-FRET ($\bar{\tau}_{on}$) (red) and low-FRET ($\bar{\tau}_{off}$) (green) interactions for each sensor design. All data are presented as mean ± s.d., where n = 3 populations of a split data set for each condition. (For interpretation of the references to colour in this figure legend, the reader is referred to the Web version of this article.)

To estimate the dwell times for high-(τ_{on}) and low-FRET (τ_{off}) states each intensity-time trace was fit with a two-state Hidden Markov Model (HMM) (Bronson et al., 2009), and the dwell times of individual events were extracted (Fig. S2A). For each of the two states, the average dwell time ($\bar{\tau}$) was then calculated by fitting an exponential decay function to the cumulative frequency of the dwell time population (see SI and Figs. S2B–S2E). These FRET-state times encompass events where the query may have instantly re-bound to the same strand, and are thus are best described as the mean first passage times between bound states (with the unbound state serving as a short-lived intermediate) (Polizzi et al., 2016). The average dwell times for high- ($\bar{\tau}_{on}$) and low-FRET ($\bar{\tau}_{off}$)

states for $Q_8C_7QS_{18}CS_3$ were 6.3 ± 1.6 s and 13.3 ± 2.2 s, respectively (Fig. 2H). Interestingly, $\bar{\tau}_{off}$ was approximately 2-fold higher than $\bar{\tau}_{on}$ (Fig. 2H) even though the query-competitor duplex was less thermodynamically stable ($T_m = 18.1\,°C$) than the query-target duplex ($T_m = 30.2\,°C$, see Table S3), suggesting that the geometry of the sensor causes the query to preferentially bind the competitor rather than the target. Together, these results suggested that single-molecule kinetic fingerprinting could be accelerated by fine-tuning sensor properties such as the thermodynamic stability of transient duplexes and the lengths of various spacers within the sensor. Considering the inverse relationship between the hybridization length of two oligonucleotides and the

specificity of the interaction (Zhang et al., 2012), we opted to keep the query-target complementarity to 8 bp while tuning other parameters like spacer and competitor lengths to shorten τ_{on} and τ_{off} and obtain more balanced distributions between FRET states.

To obtain a more balanced FRET distribution, we increased the query spacer from dT_{18} to dT_{33} (Fig. S1B). As expected, $Q_8C_7QS_{33}CS_3$ shifted towards the high-FRET state (Fig. 2D). $\overline{\tau}_{off}$ was 5.2 ± 0.9 s, a reduction of approximately 60% compared to $Q_8C_7QS_{18}CS_3$. In contrast, there was no significant change in $\overline{\tau}_{on}$ (Fig. 2H, left two panels). A possible explanation for this observation is that increasing the length of the query spacer also increases the entropic cost of query-competitor binding, reducing τ_{off}. Consistent with this hypothesis, when we reduced the query spacer to 3 nt ($Q_8C_7QS_3CS_3$), a static low-FRET behavior was observed, presumably due to the minimized entropic cost of query-competitor binding (Fig. S1B and S1E).

To further reduce dwell times, we shortened the competitor sequence from C_7 to C_6 and tested three different iSiMREPS sensors with varying query spacer lengths of dT_3, dT_{18}, and dT_{33} (Fig. 2A and S1C). As with its C_7 counterpart, $Q_8C_6QS_3CS_3$ did not show any high-FRET signal (Fig. S1F). $Q_8C_6QS_{33}CS_3$ showed a significant reduction in both τ_{on} and τ_{off} compared to its C_7 counterpart (Fig. 2E). However, $\overline{\tau}_{off}$ was reduced substantially to 0.5 ± 0.1 s, and there was a strong dominance of the high-FRET state ($\overline{\tau}_{on}$) (Fig. 2H). We obtained the most promising results from $Q_8C_6QS_{18}CS_3$ (Fig. 2A), which showed near-parity between the high- and low-FRET states (Fig. 2F) with $\overline{\tau}_{on}$ and $\overline{\tau}_{off}$ (relative to $Q_8C_7QS_{33}CS_3$) of 4.7 ± 0.7 s and 3.5 ± 0.4 s, respectively (Fig. 2H). A control experiment confirmed that $Q_8C_6QS_{18}CS_3$ showed no high-FRET signal in the absence of miR-141 (Fig. 2G). Overall, the analysis of FRET behavior and dwell time suggests that as the query spacer (QS_c) length is increased, and the competitor (C_b) length decreased, the query-target interaction is favored compared to query-competitor interaction. Since $Q_8C_6QS_{18}CS_3$ showed the best kinetic fingerprint, with short and well-balanced dwell times, this design was chosen for subsequent optimization and assay development for the rapid detection of miR-141.

3.3. Monte Carlo simulations rationalize the dependence of iSiMREPS sensor kinetics on spacer length

To better understand the effect of spacer length on iSiMREPS probe kinetics, we developed a coarse-grained Monte Carlo simulation model (see detail in SI). Our simulation results (Fig. S3) show that at very short spacer lengths, the distance between the target and query strands is large (i.e., pairing is inhibited) due to conformational rigidity of the stiff anchor duplex. Increasing spacer length up to 10 nt allows the target and query strands to interact without bending the anchor duplex. Beyond 10 nt, increasing the spacer length causes the target-query distance to gradually decrease due to the query strand's increased radius of diffusion. By contrast, the query-competitor distance decreases monotonically across all spacer lengths. These findings (Fig. S3) are in qualitative agreement with the experimental results for detecting miR-141 using the 6-nt competitor (Fig. 2); the QS_3 sensors showed that query-target interactions were unfavorable, while the QS_{18} sensors showed near-parity between the two states and the QS_{33} sensors favored query-target binding.

3.4. Optimization of an iSiMREPS sensor design for detecting ctDNA

To test for generality of the iSiMREPS approach, we next targeted a different class of nucleic acid biomarker: ctDNA. We chose an *EGFR* exon 19 deletion mutation DNA (*EGFRΔ_{exon_19}*) commonly found as fragmented ctDNA in biofluids of NSCLC patients (Fan et al., 2017). The optimized iSiMREPS sensor features the same fundamental components and architecture as the sensor design for miR-141 detection. However, it deals with the greater length and dsDNA nature of the ctDNA through two additional features. First, we added a short auxiliary probe that stably binds the extended 3' end of the forward strand of the duplex

mutant target DNA (Fig. 3A) to prevent reannealing of the complementary strand once melted during sample preparation. The auxiliary probe also aims to minimize any potential secondary structure of the target strand (Johnson-Buck et al., 2019).

Second, the DNA-based architecture of iSiMREPS sensors allows us to selectively remove the CP and QP of target-less sensors after target capture and before imaging (Fig. 1) to reduce background. To this end, we developed a two-step process that employs a pair of ssDNA "invaders" that selectively bind and disassemble target-less iSiMREPS sensors via TMSD, a strategy often displayed in dynamic DNA nanotechnology (Zhang and Seelig, 2011) (Fig. 3B). In the first step, a capture invader (CI) binds to a toehold exposed on the CP in the absence of target. Via TMSD, the CI disrupts the capture-anchor duplex to remove the CP from the surface (Fig. 3B, top panel). This first step reveals a second toehold, which is then bound by a query invader (QI) in the second step. The QI disrupts the query-anchor duplex to remove the QP and its fluorescent signal from the iSiMREPS sensor (Fig. 3B, top panel). Although these invaders are designed to work on non-target-bound probes to reduce background signals significantly, the spacer on the CP can also act as a toehold and there is a minor probability (Dunn et al., 2016) that this can lead to removal of probes from target-bound sensors (Fig. 3B, bottom panel).

We performed proof-of-concept studies for detecting *EGFRΔ_{exon_19}* using a $Q_8C_6QS_{18}CS_{19}$ sensor (Fig. 3A) modelled after the optimized sensor for miR-141 (Fig. 2A). For this sensor, we used a longer competitor spacer (CS_{19} versus CS_3) to further improve parity between the FRET states. We used a query specific to *EGFRΔ_{exon_19}* ($T_m = 23.9\,^\circ$C, Table S4) that was designed to maximize discrimination between *EGFRΔ_{exon_19}* and the off-target wild type sequence (Fig. 3A), as predicted using NUPACK (Caltech:, 2007; Zadeh et al., 2011). For optimization of sensor designs, we used a synthetic forward strand of *EGFRΔ_{exon_19}*. A pair of CI and QI strands, as shown in Fig. 3A, were designed to remove non-target-bound fluorescent probes from the surface (Fig. 3B). However, the initial design of CI contains a single mismatch in the spacer region to prevent the use of the capture spacer as a toehold (Fig. 3A).

To examine the performance of $Q_8C_6QS_{18}CS_{19}$ for detecting *EGFRΔ_{exon_19}* and to assess the efficacy of the invader strands, the preassembled sensor was first tethered to the glass coverslip and the mutant DNA target was introduced to bind the sensor probes on the surface. Next the samples were (or were not) incubated with invaders and imaged with o-TIRF. We found that invader treatment significantly reduced background signal in single-molecule intensity-time traces, resulting in a 3-fold higher S/N ratio relative to samples that were not treated with invaders (Fig. 3C and D). Exponential fitting of dwell time distributions (see SI and Fig. S4C) showed a $\overline{\tau}_{on}$ and $\overline{\tau}_{off}$ of 1.7 ± 0.1 s and 0.8 ± 0.2 s respectively, indicating some bias for the high-FRET state (Fig. 3E). These $\overline{\tau}_{on}$ and $\overline{\tau}_{off}$ are shorter than those measured for miR-141 detection under similar salt concentration and temperature. This change likely arose because the query-mutant DNA duplex ($T_m = 23.9\,^\circ$C) is less stable than query-miR-141 duplex ($T_m = 30.2\,^\circ$C). Moreover, the presence of the extra 3' sequences in the *EGFRΔ_{exon_19}* target may destabilize the interaction with the query strand slightly by introducing more electrostatic repulsion from the nearby phosphates.

To modulate the dwell times of high-(τ_{on}) and low-FRET (τ_{off}) states, we designed several additional iSiMREPS sensors. Firstly, we decreased the length of competitor spacer of $Q_8C_6QS_{18}CS_{19}$ to CS_{12} and CS_4 (Fig. S5A). We expected that decreasing the CS length would 1) increase the rate of the query–competitor interactions because of higher local effective concentrations, and 2) increase τ_{off}, making it more closely resemble the high-FRET state (τ_{on}). However, the results showed that varying the CS length had an insignificant effect on the dynamics of FRET transitions in iSiMREPS sensors (Fig. 3E and S5B). This result may be because of the relatively long QS (dT_{18}) present in this series of designs introduced substantial flexibility to all constructs, thus undercutting attempts to finely tune effective local concentrations. Secondly, we

Fig. 3. Design and optimization of iSiMREPS for detection of a ctDNA biomarker mutant DNA sequence. (**A**) Design of optimized smFRET-based iSiMREPS sensor for the detection of *EGFR* exon 19 deletion mutant DNA (*EGFRΔ*exon_19). Two invaders, which are used to remove non-target-bound fluorescent probes from the surface, are also shown. (**B**) Schematic depiction of the removal of non-target-bound fluorescent probes (top) using CI and QI, and the much slower side reaction that removes target-bound probes (bottom). Each non-target-bound sensor has an exposed 9 nt toehold on the CP that binds with CI (cyan) and initiates the toehold displacement cascade. A 3 nt toehold on the CP in target-bound sensors can also bind with CI and ultimately prevent detection of a target molecule, but this reaction occurs much more slowly due to the shorter toehold. (**C**) Comparison of single-molecule FRET traces of iSiMREPS sensor in the presence (top) or absence (bottom) of the target sequence containing the *EGFRΔ*exon_19. Background signals are significantly reduced with the application of invaders (right panel) compared to samples imaged without invader treatment (left panel). (**D**) Comparison of signal-to-noise (S/N) ratio with (cyan) and without (grey) invaders. (**E**) The average dwell times spent in the high-FRET ($\bar{\tau}_{on}$) (light red) and low-FRET ($\bar{\tau}_{off}$) (green) states for different iSiMREPS sensors designs. All data are presented as mean ± s.d., with n = 3 independent experiments. (For interpretation of the references to colour in this figure legend, the reader is referred to the Web version of this article.)

ran experiments where we increased the length of competitors of $Q_8C_6QS_{18}CS_{19}$ to C_7 and C_8 to raise the thermodynamic stability of the query–competitor interaction (Table S4). Indeed, increasing the competitor length from 6- to 8-nt increased $\bar{\tau}_{off}$ significantly (Fig. 3E), further confirming that competitor length is one of the most important parameters in iSiMREPS sensor design. Overall, the $Q_8C_6QS_{18}CS_{d=4, 12, 19}$ design, where d is the number of nucleotides in CS, worked well for *EGFRΔ*exon_19. Given the insignificant effect of CS length, $Q_8C_6QS_{18}CS_{19}$ was chosen for further assay optimization.

3.5. Denaturant (formamide)-assisted rapid detection of miRNA and ctDNA using iSiMREPS

Having optimized iSiMREPS designs for both miRNA and mutant DNA, we next sought to further accelerate sensor kinetics to increase the speed of kinetic fingerprinting. As a simple approach that maintains specificity, we chose to use the denaturant formamide, which is known to destabilize nucleic acid duplexes and decrease T_m by ~2.4–2.9 °C/ (mol L^{-1}) (Blake and Delcourt, 1996). Due to the intramolecular assembly of the iSiMREPS sensor, we still expected fast association kinetics of the probes even in the presence of denaturant.

As predicted, adding formamide (10% v/v) to the imaging buffer resulted in intensity-time traces with much shorter τ_{on} and τ_{off} for both miR-141 and *EGFRΔ*$_{exon\_19}$ (Fig. 4A and D, left panels). With a standard acquisition time of 10 s per FOV and image processing (see Tables S6 and S7), histograms of the number of binding and dissociation events (N_{b+d}) for both miR-141 and *EGFRΔ*$_{exon\_19}$ targets showed good separation from background with, but not without, 10% formamide (Fig. 4A and D, right panels).

Next, we varied the formamide volume fraction from 0% to 20% (v/ v) to minimize data acquisition time while retaining sensor function and high sensitivity. The single molecule kinetic traces showed that the τ_{on} and τ_{off} decreased with increasing formamide (Figs. S6A and S7A). The $\overline{\tau}_{on}$ and $\overline{\tau}_{off}$ gradually decreased with increasing formamide from 0 to 10% for both targets but stayed roughly constant from 10 to 20% for *EGFRΔ*$_{exon\_19}$ and 15–20% for miR-141 (Figs. S8, S9, 4B and 4E). Specifically, shifting from 0% formamide to 10% formamide decreased $\overline{\tau}_{on}$

and $\overline{\tau}_{off}$ by factors of 7 and 4.5 respectively, for miR-141 (Figs. 4B), 3.5 and 2.5, respectively, for *EGFRΔ*$_{exon\_19}$ (Fig. 4E). The differences between the two sensors are consistent with the fact that DNA-RNA duplexes are more sensitive to destabilization by formamide than DNA-DNA duplexes (Casey and Davidson, 1977). The target bound signals separated well from background at ≥10% formamide and poorly or inconsistently at 0 and 5% formamide (Figs. S6B and S7B). The standard acquisition of ~10 s per FOV obtained in iSiMREPS as assisted by 10% formamide is approximately 60-times faster than intermolecular SiMREPS approaches (Hayward et al., 2018; Johnson-Buck et al., 2015).

We next evaluated the formamide dependence of sensitivity. For miR-141 and *EGFRΔ*$_{exon\_19}$, the number of accepted traces per FOV (a measure of assay sensitivity) increased with increasing formamide up to 10%, then decreased at higher formamide concentrations (Fig. 4C and F). The accepted counts for 0 and 5% formamide likely underrepresented the number of true molecules because many target-bound sensors could not be effectively differentiated from the background in the 10 s data acquisition period (Figs. S6B and S7B). The lower number of counts observed in 15 and 20% formamide likely occurred because the reduced stability of the duplexes at these percentages decreases S/N and shortens some events to below the camera exposure time (Figs. S6C, S6D, S7C and S7D). We thus used 10% formamide during subsequent sensor optimization for maximizing sensitivity and specificity.

3.6. Use of invaders to increase the sensitivity of iSiMREPS

Our previous experiments showed that use of TMSD invaders
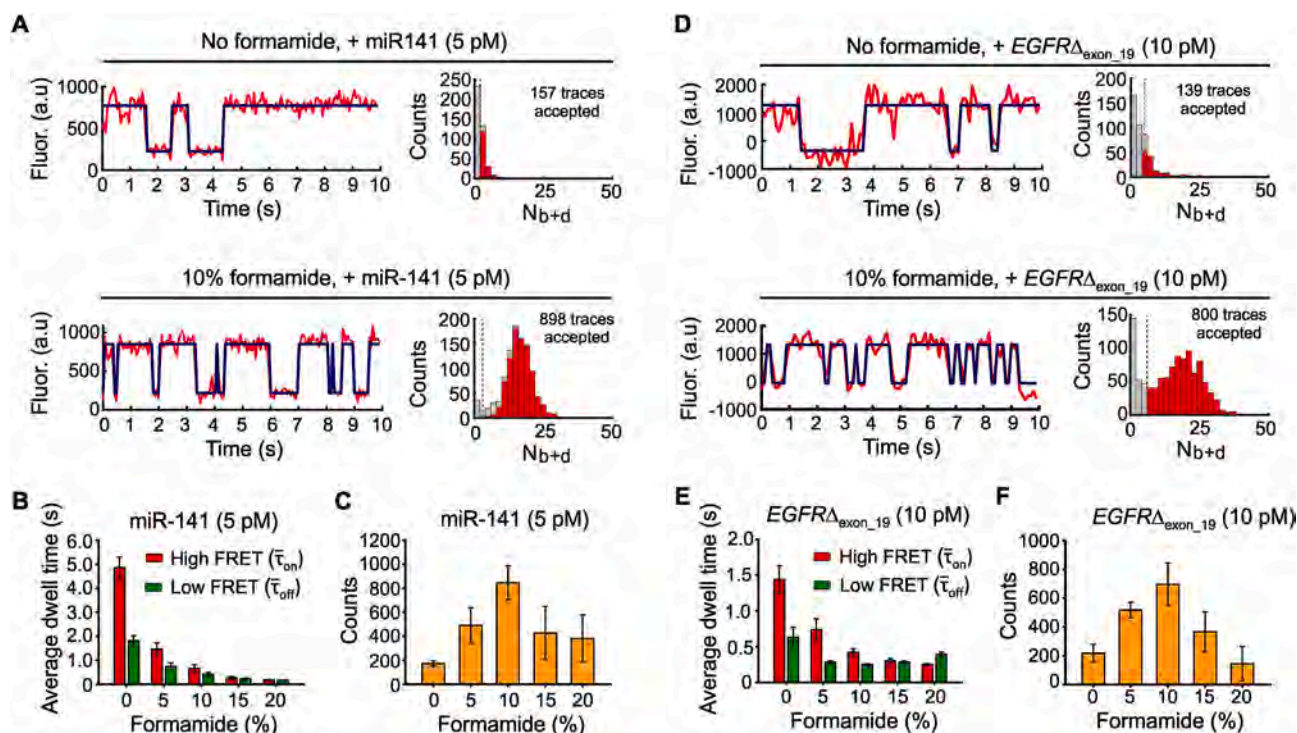
Fig. 4. The effects of formamide on iSiMREPS sensors for rapid detection of miRNA and ctDNA. (A) Representative single-molecule kinetic fingerprints and histograms of the number of candidate molecules per FOV showing a given number of binding and dissociation events (N_{b+d}) after applying thresholds for FRET intensity, S/N, and dwell times of bound and unbound states in presence of 5 pM miR-141, without (top) and with 10% (v/v) formamide (bottom). The $Q_8C_6QS_{18}CS_3$ sensor as depicted in Fig. 2A was used for this study and pre-treated with a capture invader (5′TCCGCCATATAACACTGTCTG 3′) and query invader (5′GAGTGTCCCGCGGCCCAGGA 3′) to remove non-target-bound sensors from coverslip before imaging under an objective-TIRF microscope. (B) The average dwell times for miR-141 bound state (high-FRET) ($\overline{\tau}_{on}$) and non-bound state (low-FRET) ($\overline{\tau}_{off}$) as a function of formamide (0–20%, v/v). (C) The number of candidate miR-141 bound molecules per FOV as a function of formamide after applying an optimized kinetic parameter (see SI, and Table S6). (D) Representative single-molecule kinetic fingerprints and N_{b+d} histograms per FOV in presence of 10 pM *EGFRΔ*$_{exon\_19}$ without (top) and with 10% formamide (bottom). $Q_8C_6QS_{18}CS_{19}$ sensor and invaders as depicted in Fig. 3A were used for this study. (E) The $\overline{\tau}_{on}$ and $\overline{\tau}_{off}$ for *EGFRΔ*$_{exon\_19}$ as a function of formamide (0–20%, v/v). (F) The number of candidate *EGFRΔ*$_{exon\_19}$ bound molecules per FOV as a function of formamide after applying optimized kinetic parameters (see SI, and Table S7). All data are processed at a standard data acquisition of 10s. All data are presented as mean ± s.d., where n ≥ 3 independent experiments.

significantly reduced background and improved S/N in single-molecule kinetic traces (Fig. 3). We next quantified the effect invaders have on the number of accepted counts per FOV. Firstly, we performed five experiments with the optimized $EGFR\Delta_{exon\_19}$ sensor, each pairing the identical query invader (QI) with one of five different capture invaders (CIs) shown in Fig. 5A. These CIs have different toehold and pairing region lengths. Some contain mismatches to the spacer region of the CP, which are intended to mitigate undesired displacement of target-bound sensors. We also performed a control experiment without invaders. These experiments showed that all five CIs increase the number of detected counts per FOV and decrease the number of false positives in a control without mutant DNA (Fig. 5B). However, treatment with CIs that
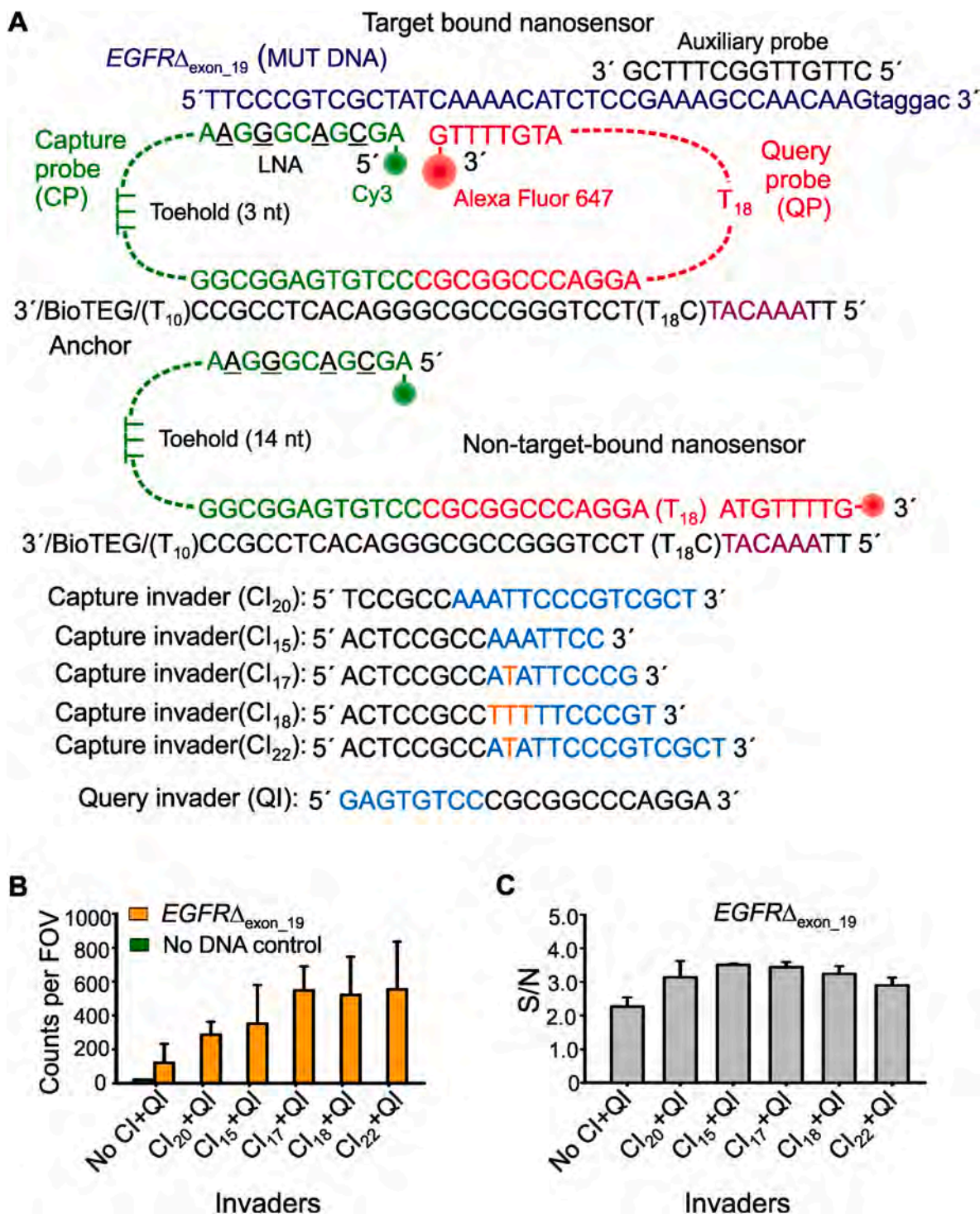
Fig. 5. Optimization of the invaders for increased sensitivity of iSiMREPS assays for nucleic acids. (**A**) Schematic of target bound and non-target-bound iSiMREPS sensors, depicting the toehold available for invader binding as well as capture invaders (CIs) of variable lengths. Cyan segments of the invaders are complementary to the exposed toeholds, while orange sequences represent the nucleotides that are mismatched between invaders and toeholds in the CP. (**B**) Number of accepted counts per FOV in the presence of $EGFR\Delta_{exon\_19}$ after application of different CIs. (**C**) S/N ratio in the candidate target bound molecules after application of different CLs. All data are presented as the mean ± s.d. of n = independent experiments. (For interpretation of the references to colour in this figure legend, the reader is referred to the Web version of this article.)

contain one or more mismatches (CI_{17}, CI_{18}, and CI_{22}) with the capture probe's 3 nt spacer showed more accepted traces and, surprisingly, improved S/N compared to treatment with fully complementary CIs (CI_{20} and CI_{15}) (Fig. 5B and C, and S10). These results suggest that fully complementary CIs cause unwanted removal of target-bound probes. Overall, treatment with CI_{17} and QI performed the best, increasing the number of accepted traces ~4.5-fold compared to assays without invaders (Fig. 5B and C). This strategy was also tested and optimized for the detection of miR-141 (Fig. S11); the best-performing CI had a mismatch and exhibited a ~3.5-fold increase in accepted traces and improved S/N (Fig. S11).

3.7. Sensitivity and specificity of detecting EGFR exon 19 deletion mutation DNA and miR-141

To further improve $EGFR\Delta_{exon\_19}$ detection sensitivity, we next optimized iSiMREPS preparation procedures and assay conditions (e.g., sensor concentration, invaders, target incubation time) (Fig. S12). Since $EGFR\Delta_{exon\_19}$ exists in double-stranded (ds) DNA form in biofluids, the target was thermally denatured at 90 °C for 3 min and cooled at room temperature in the presence of an auxiliary probe that binds stably to the forward strand of mutant DNA (Fig. 3A). During this step, the poly-dT (dT_{30}) was included in high molar excess as a carrier (Hayward et al., 2018). The auxiliary probe and dT_{30} help keep the capture region of the target DNA in an ssDNA form, permitting efficient and specific capture.

Experiments using mutant ssDNA and dsDNA treated with the above denaturation steps showed similar results (Fig. 6A). The iSiMREPS assay for the $EGFR\Delta_{exon\_19}$ dsDNA was found to have a LOD of 3.2 fM in buffer (Fig. 6B) and a linear dynamic range spanning ~4 orders of magnitude (Fig. S13A), a ~1.5-fold improvement over conventional SiMREPS (Hayward et al., 2018). $EGFR\Delta_{exon\_19}$ detection in the presence and absence of a large (10^{5-6}-fold) excess of wild-type DNA showed 99.9996–99.9999% specificity for, permitting mutant detection at an allelic fraction of 0.001–0.0001% (Fig. 6C and S14 and Table S8). The miR-141 assay exhibited an LOD of 3.4 fM (Fig. 6D) with a dynamic range of approximately 3.2 orders of magnitude (Fig. S13B), a 1.2-fold improvement over conventional SiMREPS (Johnson-Buck et al., 2015), with similar sensitivity in one 60th of the time. Overall, iSiMREPS shows slightly lower sensitivity than some existing technologies for detecting nucleic acids like droplet digital PCR (Mestdagh et al., 2014; Milbury et al., 2014) and NGS (Postel et al., 2018). However, it exhibits superior specificity, comparable or better dynamic range than existing single-nucleic acid detection techniques (Gilboa et al., 2020) and achieves rapid detection with lower risk of cross-contamination, an elimination of sequence bias or inhibition due to enzymatic amplification, and a lack of need for purification, complex sample preparations or enzymatic reactions compared to existing techniques.
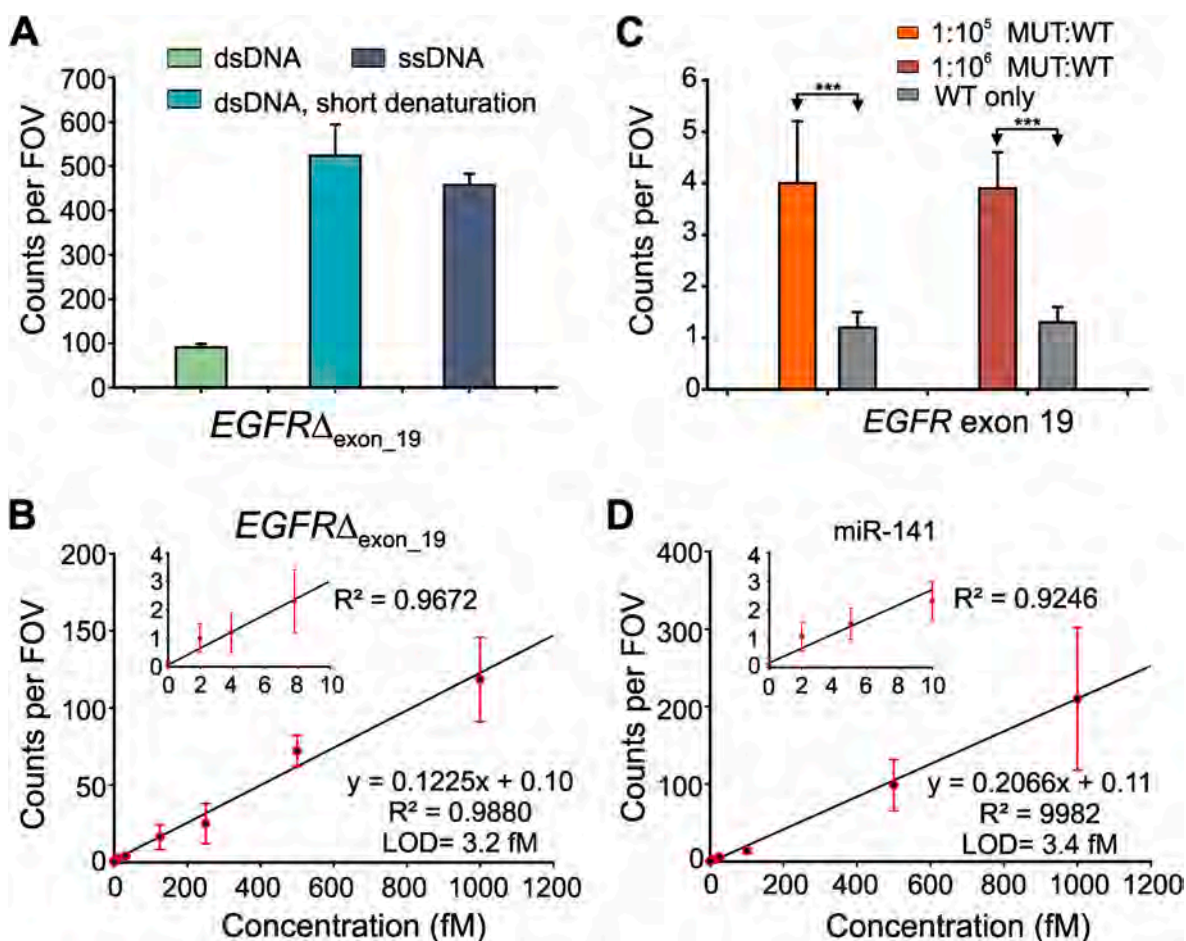
Fig. 6. Standard curve and specificity of detecting *EGFR* exon 19 deletion ($EGFR\Delta_{exon\_19}$) and miR-141. (**A**) Effect of short thermal denaturation on the accepted counts of $EGFR\Delta_{exon\_19}$ duplex DNA (dsDNA). (**B**) Standard curve for $EGFR\Delta_{exon\_19}$ showing a LOD of 3.2 fM. Linear fits were constrained to a y-intercept of accepted counts at 0 fM. (**C**) Comparison of counts from low MUT allelic fraction and WT only conditions for determining specificity. Triple asterisks indicate the significant differences at 95% confidence levels as assessed using a two-tailed, unpaired *t*-test and showed a specificity of 99.9996–99.9999% over the MUT fraction of 0.001–0.0001%. (**D**) Standard curve for miR-141 showing a LOD of approximately 3.4 fM. Linear fits were constrained to a y-intercept of accepted counts at 0 fM. All data are presented as mean ± s.d., where n ≥ 3 independent experiments.

4. Conclusions

In this study, we developed a novel intramolecular smFRET-based kinetic fingerprinting technique (iSiMREPS) using a dynamic DNA nanosensor that enables rapid, highly sensitive and ultraspecific detection of diverse nucleic acid biomarkers. iSiMREPS's intramolecular sensor design allows for accelerated kinetic fingerprinting by dramatically increasing the local effective concentration of probes and target. We optimized functional features of iSiMREPS such as the hybridization length of the query probe to the target and competitor, as well the length of the spacer in the query probe, to obtain sensor designs capable of quick fingerprint generation. We then demonstrated that the denaturant formamide further accelerates probe-target kinetics and, because iSiMREPS's unique features permit sensors to retain high-affinity capture of single oligonucleotides under such conditions, fingerprint generation was achieved in 10 s per FOV. Moreover, the sensor design was amenable to a TMSD strategy that removed non-target bound sensors, nearly eliminating background noise. Yet, despite its several advances iSiMREPS is susceptible to fluorophore photobleaching and its sensitivity is, as with all surface-based assays, limited by the diffusion of the target molecules to the surface. In the future, sensitivity may be further improved by increasing surface concentration with a pre-concentration technique or by recording additional FOVs, a prospect possible because of the short acquisition times. Additionally, faster cameras with higher laser intensities or sensor designs that withstand higher formamide concentrations and/or temperatures may permit even faster detection speeds. Overall, iSiMREPS has demonstrated the analytical performance necessary for advanced applications in the liquid biopsy field with greater speed and potential for higher sample throughput. We anticipate that iSiMREPS can be further generalized for the rapid, highly sensitive and specific analysis of diverse analytes including nucleic acids, proteins, and small molecules in a spatially addressable microarray format.

Funding sources

CRediT authorship contribution statement

Kunal Khanna: Conceptualization, Investigation, Writing – original draft, Writing – review & editing, Visualization, Validation, Formal analysis, Methodology. **Shankar Mandal:** Conceptualization, Investigation, Writing – original draft, Writing – review & editing, Visualization, Validation, Formal analysis, Methodology. **Aaron T. Blanchard:** Writing – review & editing, Formal analysis, Methodology, Visualization. **Muneesh Tewari:** Conceptualization, Supervision, Funding acquisition, Writing – review & editing. **Alexander Johnson-Buck:** Conceptualization, Writing – review & editing, Software, Funding acquisition, Supervision. **Nils G. Walter:** Conceptualization, Supervision, Funding acquisition, Writing – review & editing.

Data availability

The data discussed in this publication will be made available upon request.

Declaration of competing interest

Appendix B. Supplementary data

Supplementary data to this article can be found online at https://doi.org/10.1016/j.bios.2021.113433.

References

Akkilic, N., Geschwindner, S., Höök, F., 2020. Biosens. Bioelectron. 151, 9.
Anfossi, S., Babayan, A., Pantel, K., Calin, G.A., 2018. Nat. Rev. Clin. Oncol. 15, 541–563.
Blake, R.D., Delcourt, S.G., 1996. Nucleic Acids Res. 24, 2095–2103.
Bronson, J.E., Fei, J., Hofman, J.M., Gonzalez Jr., R.L., Wiggins, C.H., 2009. Biophys. J. 97, 3196–3205.
Bryant, R.J., Pawlowski, T., Catto, J.W., Marsden, G., Vessella, R.L., Rhees, B., Kuslich, C., Visakorpi, T., Hamdy, F.C., 2012. Br. J. Canc. 106, 768–774.
Caltech, 2007.
Casey, J., Davidson, N., 1977. Nucleic Acids Res. 4, 1539–1552.
Cohen, L., Hartman, M.R., Amardey-Wellington, A., Walt, D.R., 2017. Nucleic Acids Res. 45 e137-e137.
Crowley, E., Di Nicolantonio, F., Loupakis, F., Bardelli, A., 2013. Nat. Rev. Clin. Oncol. 10, 472–484.
Dunn, K.E., Trefzer, M.A., Johnson, S., Tyrrell, A.M., 2016. Sci. Rep. 6, 29581.
Fan, G., Zhang, K., Ding, J., Li, J., 2017. Oncotarget 8, 33922–33932.
Gazdar, A.F., 2009. Oncogene 1, 198.
Gilboa, T., Garden, P.M., Cohen, L., 2020. Anal. Chim. Acta 1115, 61–85.
Hayward, S.L., Lund, P.E., Kang, Q., Johnson-Buck, A., Tewari, M., Walter, N.G., 2018. J. Am. Chem. Soc. 140, 11755–11762.
Heitzer, E., Ulz, P., Geigl, J.B., 2015. Clin. Chem. 61, 112–123.
Johnson-Buck, A., Li, J., Tewari, M., Walter, N.G., 2019. Methods 153, 3–12.
Johnson-Buck, A., Su, X., Giraldez, M.D., Zhao, M., Tewari, M., Walter, N.G., 2015. Nat. Biotechnol. 33, 730–732.
Li, F., Tang, Y., Traynor, S.M., Li, X.-F., Le, X.C., 2016. Anal. Chem. 88, 8152–8157.
Li, Z., Zhou, X., Li, L., Liu, S., Wang, C., Yu, C., Su, X., 2018. Anal. Chem. 90, 6804–6810.
Ma, F., Li, Y., Tang, B., Zhang, C.-y., 2016. Acc. Chem. Res. 49, 1722–1730.
Mestdagh, P., Hartmann, N., Baeriswyl, L., Andreasen, D., Bernard, N., Chen, C., Cheo, D., D'Andrade, P., DeMayo, M., Dennis, L., Derveaux, S., Feng, Y., Fulmer-Smentek, S., Gerstmayer, B., Gouffon, J., Grimley, C., Lader, E., Lee, K.Y., Luo, S., Mouritzen, P., Narayanan, A., Patel, S., Peiffer, S., Rüberg, S., Schroth, G., Schuster, D., Shaffer, J.M., Shelton, E.J., Silveria, S., Ulmanella, U., Veeramachaneni, V., Staedtler, F., Peters, T., Guettouche, T., Wong, L., Vandesompele, J., 2014. Nat. Methods 11, 809–815.
Milbury, C.A., Zhong, Q., Lin, J., Williams, M., Olson, J., Link, D.R., Hutchison, B., 2014. Biomol. Detect. Quantif. 1, 8–22.
Mitchell, P.S., Parkin, R.K., Kroh, E.M., Fritz, B.R., Wyman, S.K., Pogosova-Agadjanyan, E.L., Peterson, A., Noteboom, J., O'Briant, K.C., Allen, A., Lin, D.W., Urban, N., Drescher, C.W., Knudsen, B.S., Stirewalt, D.L., Gentleman, R., Vessella, R. L., Nelson, P.S., Martin, D.B., Tewari, M., 2008. Proc. Natl. Acad. Sci. U.S.A. 105, 10513–10518.
Murphy, M.C., Rasnik, I., Cheng, W., Lohman, T.M., Ha, T., 2004. Biophys. J. 86, 2530–2537.
Polizzi, N.F., Therien, M.J., Beratan, D.N., 2016. Isr. J. Chem. 56, 816–824.
Postel, M., Roosen, A., Laurent-Puig, P., Taly, V., Wang-Renault, S.F., 2018. Expert Rev. Mol. Diagn 18, 7–17.
Potapov, V., Ong, J.L., 2017. PloS One 12 e0169774.
Schmitt, M.W., Kennedy, S.R., Salk, J.J., Fox, E.J., Hiatt, J.B., Loeb, L.A., 2012. Proc. Natl. Acad. Sci. U. S A 109, 14508–14513.
Schwarzenbach, H., Hoon, D.S., Pantel, K., 2011. Nat. Rev. Canc. 11, 426–437.
Wang, J.S., Zhang, D.Y., 2015. Nat. Chem. 7, 545–553.
Zadeh, J.N., Steenberg, C.D., Bois, J.S., Wolfe, B.R., Pierce, M.B., Khan, A.R., Dirks, R.M., Pierce, N.A., 2011. J. Comput. Chem. 32, 170–173.
Zhang, D.Y., Chen, S.X., Yin, P., 2012. Nat. Chem. 4, 208–214.
Zhang, D.Y., Seelig, G., 2011. Nat. Chem. 3, 103–113.

Supplementary Information

Rapid kinetic fingerprinting of single nucleic acid molecules by a FRET-based dynamic nanosensor

*Kunal Khanna[a,2], Shankar Mandal[a,2], Aaron T. Blanchard[a,b,c], Muneesh Tewari[b,d,e,f], Alexander Johnson-Buck[a,d,e,1,**], and Nils G. Walter[a,e,f,*]*

[a] Single Molecule Analysis Group, Department of Chemistry, University of Michigan, Ann Arbor, Michigan, 48109, United States

[b] Department of Biomedical Engineering, University of Michigan, Ann Arbor, Michigan, 48109, United States

[c] Michigan Society of Fellows, University of Michigan, Ann Arbor, Michigan 48109, United States

[d] Department of Internal Medicine, Division of Hematology/Oncology, University of Michigan, Ann Arbor, Michigan, 48109, United States

[e] Center for RNA Biomedicine, University of Michigan, Ann Arbor, Michigan, 48109, United States

[f] Center for Computational Medicine and Bioinformatics, University of Michigan, Ann Arbor, Michigan, 48109, United States

[*] Corresponding author. Single Molecule Analysis Group, Department of Chemistry, University of Michigan, Ann Arbor, MI, 48109, United States.
[**] Corresponding author. Single Molecule Analysis Group, Department of Chemistry, University of Michigan, Ann Arbor, MI, 48109, United States.
Email addresses: alebuck@umich.edu (A. Johnson-Buck), nwalter@umich.edu (N.G. Walter)

[2] These authors contributed equally to this work

[1] Present Address: Alexander Johnson-Buck, aLight Sciences, Inc., 333 Jackson Plz Suite 460, Ann Arbor, Michigan, 48103, United States

Table of contents

1. Supplementary texts

1.1 Preparation of slides, coverslips, and sample cells

Single-molecule fluorescence microscopy experiments were performed using either an objective-TIRF or a prism-TIRF microscope, which required different protocols for preparing slides or coverslips and sample cells as previously described (Abelson et al., 2010; Johnson-Buck et al., 2019). Objective-TIRF coverslips and imaging cells were prepared by following three basic steps: cleaning the coverslip to remove organic residues from surface, passivating the surface with affinity tags, and preparing the sample cells by attaching cut pipette tips as described previously (Chatterjee et al., 2020; Hayward et al., 2018). Briefly, VWR No. 1.5, 24×50 mm coverslips (VWR, catalog no. 48393-241) were cleaned following either one of two procedures. In one cleaning procedure, the coverslips were cleaned by applying plasma for 3 min and then washed two times with acetone. In the second cleaning procedure, the coverslips were first sonicated for 10 min in acetone, then sonicated in 1M KOH for 20 min, and finally were treated with "base piranha" solution consisting of 14.3% v/v of 28-30 wt% NH_4OH, and 14.3% v/v of 30-35 wt% H_2O_2 that was heated to 70-80°C before immersing the slide in it as previously described (Chatterjee et al., 2020). Following either cleaning procedure, coverslips were then modified to present surface amines by mounting them in a coplin jar and submerging them in a 2% v/v solution of (3-aminopropyl) triethoxysilane (APTES) (Sigma-Aldrich, catalog no. A3648-100ML) in acetone for 10 min, sonicating the jar for 1 min, incubating for another 10 min, rinsed twice with acetone, rinsed five times with water, and dried with nitrogen. Slides were then functionalized by sandwiching a 1:10 or 1:100 mixture of biotin-PEG-succinimidyl valerate and methoxy-PEG-succinimidyl valerate (Laysan Bio, Inc. catalog no. BIO-PEG-SVA-5K-100MG & MPEG-SVA-5K-1g) in 0.1M $NaHCO_3$ with a final mPEG concentration of 0.25 mg/μL and a final biotin PEG concentration of 0.0025 or 0.025 mg/μL for 1:100 or 1:10 mixtures, respectively, between pairs of coverslips. To reduce nonspecific binding of nucleic acids to the surface, the remaining surface amines were quenched by sandwiching ~80 μL of 0.03 mg/μL disulfosuccinimidyltartrate (Soltec Ventures, catalog no. CL107) in 1M $NaHCO_3$ between pairs of coverslips. Finally, the coverslips were dried completely under nitrogen flow and stored in the dark under air for further use for up to 3 weeks. The sample cells were prepared prior to the single-molecule experiments using 20 μL pipet tips (ART low retention, Thermo Scientific). Specifically, a razor blade was used to cut through the diameter of a pipette tip ~2 cm from the wide end of the pipette tip and the noncut base was attached to the functionalized coverslip via epoxy (Ellsworth adhesives, hardman double, catalog no. 4001) (Hayward et al., 2018). Four pipette tips were generally attached to each coverslip in this manner. The 1:10 PEG ratio coverslips were used for objective-TIRF miR-141 optimization experiments and the 1:100 PEG ratio was used for all optimization and quantification experiments for *EGFR* exon 19 deletion mutant DNA (*EGFR*Δexon_19) and quantification experiments only for miR-141RNA. Additionally, all objective-TIRF miR-141 quantification experiments used plasma cleaning while all *EGFR*Δexon_19 experiments used piranha cleaning and miR-141 optimization used mostly piranha with some plasma cleaning. Both cleaning protocols showed very similar analytical performance (Fig. S15). For prism TIRF experiments, the fluidic sample cells were

constructed using two pieces of double-sided tape sandwiched between a microscope slide and glass coverslip (VWR 22×30 mm). Each microscope slide had a hole on each of two ends, which was connected to Tygon tubing for exchanging sample solutions and buffers. Prior to assembly of the sample cell, the microscope slide's surface was cleaned using an aqueous solution of "base piranha" as described above. The microscope slides were often reused by heating the slides in warm to boiling water to loosen the glue and remove the coverslip, followed by removal of all remaining residue with a razor blade and subsequent Alconox paste and base piranha cleaning.

1.2 Prism-type TIRF iSiMREPS assay for detection of miR-141

To detect miR-141 using a prism-TIRF microscope (Fig. 2), a fluidic sample cell was first passivated by injecting 150 µL of 1 mg/mL biotin-BSA (Thermo Fischer, 25mg ImmunoPure) for 10 min to coat the slide surface with biotin-BSA. The chamber was then washed out with T50 (10 mM Tris pH 8.0 at 25°C, 50 mM NaCl) and 150 µL of streptavidin at 1mg/mL concentration was flowed into the chamber, and the streptavidin was allowed to incubate for 10 min to bind with the biotin-BSA. The unbound streptavidin was then washed out with 4× PBS (Phosphate-buffered saline, pH 7.4 at 25°C). Next, 150 µL of preassembled iSiMREPS sensors bound with miR-141 were injected into the chamber for tethering onto the slide surface via biotin-streptavidin linkages. The sensors used for this step were assembled by combining the anchor, capture, and query probes as well as the miR-141 target at 1.000:1.125:1.125:1.250 ratios respectively at approximately 100 pM final concentration in 150 µL solutions in 4× PBS buffer. After combining, the sensors were heated at 70°C for 7 min in a metal bath and then cooled at room temperature for 20 min. To prolong the lifetimes of fluorophores and thus obtain more accurate measurements of the FRET signals, an imaging buffer containing an oxygen scavenger system (OSS) consisting of 1 mM Trolox, 5 mM 3,4-dihydroxybenzoate, and 50 nM protocatechuate dioxygenase in 4× PBS was injected into the chamber prior to imaging under a prism-TIRF microscope.

1.3 Exponential fitting of the cumulative frequency of dwell times

Average dwell times for a given experiment were processed using a custom MATLAB (version 2019a or later) script. The script first determined the cumulative frequency of all the dwell times for a given state using bins the size of the camera exposure time (0.06-0.1 s). This cumulative frequency was then fit to either a single exponential function (*Equation S1*) or a double exponential function (*Equation S2*):

$$y = ae^{-x/\tau} + c \qquad\qquad\qquad (S1)$$
$$y = ae^{-x/\tau 1} + be^{-x/\tau 2} + c \qquad\qquad\qquad (S2)$$

where a, b, c, τ, $\tau 1$ and $\tau 2$ are fit parameters. The coefficients a and b are used to fit the function and for the double exponential, determine the weight of each term for plotting, and obtaining average dwell times. The coefficient τ describes, for the single exponential fit, the average dwell time for a given event. The coefficients $\tau 1$ and $\tau 2$ describe, for the double exponential fit, the average dwell time for shorter- and

longer-lived populations of events, respectively. The coefficient c is a constant the gives the y-intercept for the equation.

For each dataset, the cumulative frequency was first fit to the single exponential fitting function. This fit was then kept if the sum squared error < 0.05 and the R^2 > 0.98 for detecting miR-141 and the sum squared error < 0.08 and the R^2 > 0.96 for detecting *EGFR* exon 19 deletion mutant DNA (*EGFR*$_{\Delta exon\_19}$), which indicated a good fit and suggested that the coefficient t was an accurate average dwell time. If these conditions were not met, a double exponential function (equation S2) was used instead, and the average dwell time was calculated as $\tau = (a\tau1 + b\tau2)/(a + b)$. This equation calculated a weighted average of both populations that was reported as the average dwell time for the entire data set.

1.4 Statistical mechanical simulations of iSiMREPS sensors

Simulations were performed using a Monte Carlo simulation method described by Becker, Rosa, and Everaers (Becker et al., 2010). In this method, each ssDNA nucleotide (nt) or dsDNA base pair (bp) was represented as a point at fixed distance from its neighbors, h (0.6 nm/nt for ssDNA (Saleh et al., 2009) or 0.34 nm/bp for dsDNA (Marko and Siggia, 1995)), and then a series of 10^7 iterations were applied to the construct via the Metropolis-Hastings algorithm. Each iteration consisted of a pivot attempt, which entails selection of a random point in the construct, followed by a counterclockwise rotation of all downstream points (where upstream means closer to the point at which the construct is anchored to the surface) around a random axis by an angle randomly sampled from the range $\pm 50°$. The construct's post-pivot free energy, G, was calculated as the sum of the bending energy of all non-terminal points. The bending energy for the ith non-terminal point (e.g., a point that is bound to at least two additional points), g_i, with 3D coordinate vector r_i is:

$$g_i = -k_{s,i} \frac{(r_i - r_{i\leftarrow}) \cdot (r_i - r_{i\rightarrow})}{|r_i - r_{i\leftarrow}||r_i - r_{i\rightarrow}|} \tag{S3}$$

where $k_{s,i}$ is the point's bending spring constant, which is related to the persistence length, L_p (1.4 nm for ssDNA(Chen et al., 2012) or 53 nm for dsDNA(Marko and Siggia, 1995), via the relation

$$L_p = \frac{-h}{\ln\left(coth(k_s) - \frac{1}{k_s}\right)} \tag{S4}$$

and $r_{i\leftarrow}$ and $r_{i\rightarrow}$ are the 3D coordinate vectors for the nearest upstream and downstream points, respectively. (Note that for single-stranded RNA in the miR-141 design, we used $L_p = 0.8\,nm$ and $h = 0.67\,nm$) (Seol et al., 2004). Next, G was calculated as $G = \sum g_i$ and the change in G from the last iteration, ΔG, was used to determine whether the pivot is accepted. Specifically, the pivot was accepted if $\Delta G < 0$ or, in the scenario that $\Delta G > 0$, if $\exp(-\Delta G) > R$, where R is a randomly generated number sampled from the range of 0 to 1. To reflect attachment of the construct to a surface, G was set to ∞ if any point in the construct exhibited a z-position below 0. Regardless of whether or not the pivot was accepted, the inter-strand distance was calculated at the end of each iteration as the average of the

distances between the pairs of nucleotides that pair together to form the query-target duplex or the competitor-query duplex.

1.5 Optimization of iSiMREPS sensor concentration, invaders, and target incubation time to increase the sensitivity of detecting *EGFR* exon 19 deletion mutant DNA (*EGFR*Δ$_{exon\_19}$).

The iSiMREPS sensor is used to count surface-immobilized analyte molecules via a TIRF microscopy setup. Thus, the sensitivity of iSiMREPS is limited by the diffusion of target molecules to the surface, as well as the kinetics and thermodynamics of binding between the target and capture probe. The number of surface-immobilized target molecules can be enhanced by increasing the density of sensors on the surface as well incubating target solution for a longer duration. However, higher sensor density results in higher background signal, which can be addressed with higher invader concentration and/or longer invader incubation time. To increase the sensitivity of iSiMREPS, we therefore tested the performance of the sensor $Q_8C_6QS_{18}CS_{19}$ with different probe concentrations, invaders, and target incubation times.

First, the performance of the sensor was tested using 10, 25, and 50 nM sensor to detect 10 pM *EGFR* exon 19 deletion mutant DNA (*EGFR*Δ$_{exon\_19}$). The target was incubated for 90 min and pretreated with 2.5 µM invaders for 20 min to remove non-target bound sensors before imaging. The results showed that S/N values in the target bound traces decreased as sensor concentration increased (Fig. S12A). However, the number of accepted traces per FOV was highest when 25 nM sensor was used (Fig. S12A). This can potentially be explained as follows: with 10 nM sensor, the surface density of sensor was insufficient to efficiently capture target molecules, resulting in low counts; with 50 nM sensor, the imaging surface was saturated with target bound molecules, resulting in high background. Since 25 nM probe showed good S/N and more accepted traces per FOV, we considered this concentration for further optimization of assay conditions.

Next, we varied the incubation time of invaders (5, 10, 20, 25, and 30 min) while holding all other parameters and assay conditions equal. The number of accepted counts increased roughly linearly with the invader's incubation time and flatlined at 20 min. Therefore, 20 min was chosen as the optimized invader incubation time (Fig. S12B). Finally, we tested the effect of target incubation time on the sensitivity of the sensor. We varied the target incubation time (30, 60, 90 and 120 min) while holding all other parameters and assay conditions equal. The results showed that the number of accepted traces increased with the target incubation time, peaked 90 min, declined at 120 min (Fig. S12C). It is possible that at 120 min, some sensors dissociated from the surface. Therefore, a target incubation time of 90 min was chosen for further experimentation.

6

1.6 Calculation of specificity for detection of *EGFR* exon 19 deletion mutant DNA (*EGFR*Δ_exon_19).

      The specificity of the iSiMREPS assay for detecting *EGFR* exon 19 deletion mutant (MUT) DNA in the presence of wild-type (WT) DNA was calculated based on a previously-published protocol(Hayward et al., 2018). Briefly, to determine specificity, 500 fM MUT DNA was spiked into 50 or 500 nM WT DNA to obtain a mutant allelic fraction of 0.001 or 0.0001%, respectively. These samples were analyzed using an objective-type TIRF microscope as described in the Methods section in the main text. MUT-free samples with 50 or 500 nM WT were used as controls. The specificity was then calculated from the number of true negative (*TN*) and false positive (*FP*) counts using the following relationship.

$$Specificity = \frac{TN}{TN+FP} \qquad\qquad (S5)$$

TN is equal to the number of WT molecules within the field of view that are not detected as MUT and *FP* is equal to the number of false positives in a WT-only experiment.

$$TN = (Number\ of\ WT\ molecules\ in\ FOV) - FP \qquad\qquad (S6)$$

      In an iSiMREPS assay, the number of WT molecules per field of view can be estimated by assuming that the kinetics of capture are identical for MUT and WT molecules with the equation below.

$$Number\ of\ WT\ molecules\ in\ FOV = TP \times (C_{WT}/ C_{MUT}) \qquad\qquad (S7)$$

C_{WT} and C_{MUT} are the concentrations of WT and MUT molecules, respectively, and *TP* is the number of true positives within the field of view.

Number of true positives (TP) in FOV = (Number of counts in MUT + WT) – (Number of counts in WT-only)   (S8)

$$TN = TP \times (C_{WT}/C_{MUT}) - FP \qquad\qquad (S9)$$

By substituting equation (S9) into equation (S5), we obtain

$$Specificity = 1 - \frac{FP}{TP \times (C_{WT}/C_{MUT})} \qquad\qquad (S10)$$

1.7 Processing and analysis of prism-TIRF data

      The prism-TIRF movies were processed with MATLAB scripts that detected areas of higher intensity that correspond to potential molecules and used a bead mapping procedure (Abelson et al., 2010) to pair donor and acceptor signals in both channels coming from the same molecules. These scripts generated trace files that were analyzed with other scripts, where traces that showed transitions between FRET states (indicative of fingerprint generation) were selected for further analysis of their kinetics and FRET distribution. The criteria for which traces were accepted or rejected is outlined in Table S5. The traces, once selected, were then further processed with MATLAB scripts to obtain FRET values and time data that could be inputted into QuB (University of Buffalo software). QuB was then used to create an idealized hidden Markov model (HMM) (Bronson et al., 2009) to assign FRET states for all traces at each time. Idealized trace data from QuB was then further processed with MATLAB scripts to do two things: (1) Obtain dwell times in the low and high-FRET states and an average dwell time per state through cumulative frequency exponential fitting (see SI above, and Fig. S2), and (2) Obtain transition occupancy density plots (TODPs) which show the frequency of molecules exhibiting transitions between

particular pairs of FRET states (Blanco and Walter, 2010). These average dwell times and TODPs were used to evaluate the sensor performance.

2. Supporting Tables

Table S1. The list of oligonucleotides used for detection of miR-141.

ID	Sequence: 5´-3´	Usage
miR-141	UAACACUGUCUGGUAAAGAUGG	All sensors
Capture_miR-141	/5Cy3/C+A+GAC+A+GTGTTATTTGGCGGAGTGTCC	All sensors
Query_Q_8QS_3	CGCGGCCCAGGATTTCCATCTTT/3AlexF647N/	All sensors with Q_8QS_3
Query_Q_8QS_{18}	CGCGGCCCAGGATTTTTTTTTTTTTTTTTCCATCTTT /3AlexF647N/	All sensors with Q_8QS_{18}
Query_Q_8QS_{33}	CGCGGCCCAGGATTTTTTTTTTTTTTT TTTTTTTTTTTTTTTTTTCCATCTTT/3AlexF647N/	All sensors with Q_8QS_{33}
Anchor_C_6CS_3	TTAGATGGTTTTCCTGGGCCGCGGGACACTCC GCCTTTTTTTT/3Bio-TEG/	All sensors with C_6CS_3
Anchor_C_7CS_3	TTAAGATGGTTTTCCTGGGCCGCGGGACACTCC GCCTTTTTTTT/3Bio-TEG/	All sensors with C_7CS_3
Anchor_C_8CS_3	TTTCCTGGGCCGCGGGACACTCCGCCTTTTTTT T/3Bio-TEG/	All sensors with C_8CS_3
CI_{mis}	TCCGCCATATAACACTGTCTG	Removes capture probe from non-target-bound sensor. Sequence has mismatch in area that binds to capture linker.
CI_{full}	TCCGCCAAATAACACTGTCTG	Removes capture probe from non-target-bound sensor. Sequence is fully complementary to its target on the capture probe.
QI	GAGTGTCCCGCGGCCCAGGA	Removes query probe from non-target-bound sensor

Table S2. The list of oligonucleotides used for detection of *EGFR* exon19 deletion mutant DNA (*EGFR*Δ$_{exon\_19}$).

ID	Sequence: 5´-3´	Usage
Capture_ Exon 19	/5AmMC6/AG+CG+ACG+GG+AATTTGGCGGAGTGTCC	All sensors
Query_Q$_8$QS$_{18}$	CGCGGCCCAGGATTTTTTTTTTTTTTTTTATGTTTTG/3AlexF647N/	All sensors with Q$_8$QS$_{18}$
Anchor_C$_6$CS$_4$	TTAAACATCTTTTCCTGGGCCGCGGGACACTCCGCCTTTTTTTT/3Bio-TEG/	Sensor Q$_8$C$_6$QS$_{18}$CS$_4$
Anchor_C$_6$CS$_{12}$	TTAAACATCTTTTTTTTTTTCCTGGGCGCGGGACACTCCGCCTTTTTTTT/3Bio-TEG/	Sensor Q$_8$C$_6$QS$_{18}$CS$_{12}$
Anchor_C$_6$CS$_{19}$	TTAAACATCTTTTTTTTTTTTTTTTTTCCTGGGCCGCGGGACACTCCGCCTTTTTTTT/3Bio-TEG/	Sensor Q$_8$C$_6$QS$_{18}$CS$_{19}$
Anchor_C$_7$CS$_{19}$	TTAAAACATCTTTTTTTTTTTTTTTTTTTTCCTGGGCCGCGGGACACTCCGCCTTTTTTTT/3Bio-TEG/	Sensor Q$_8$C$_7$QS$_{18}$CS$_{19}$
Anchor_C$_8$CS$_{19}$	TTACAAACATCTTTTTTTTTTTTTTTTTTTCCTGGGCCGCGGGACACTCCGCCTTTTTTTT/3Bio-TEG/	Sensor Q$_8$C$_8$QS$_{18}$CS$_{19}$
EGFR exon 19 del MUT_ FW	TTCCCGTCGCTATCAAGACATCTCCGAAAGCCAACAAGTAGGAC	FW and Rev strands were annealed to prepare dsDNA. FW strand was detected
EGFR exon 19 del MUT_Rev	GTCCTACTTGTTGGCTTTCGGAGATGTCTTGATAGCGACGGGAA	
EGFR exon 19 WT_FW	TTCCCGTCGCTATCAAGGAATTAAGAGAAGCAACATCTCCGAAAGCCAACAAGTAGGAC	FW and Rev strands were annealed to prepare dsDNA. FW strand was detected
EGFR exon 19 WT_Rev	GTCCTACTTGTTGGCTTTCGGAGATGTTGCTTCTCTTAATTCCTTGATAGCGACGGGAA	
CI$_{20}$	TCCGCCAAATTCCCGTCGCT	Removes non-target-bound capture probe
CI$_{15}$	ACTCCGCCAAATTCC	Removes non-target-bound capture probe
CI$_{17}$	ACTCCGCCATATTCCCG	Removes non-target-bound capture probe
CI$_{18}$	ACTCCGCCTTTTTCCCGT	Removes non-target-bound capture probe
CI$_{22}$	ACTCCGCCATATTCCCGTCGCT	Removes non-target-

		bound capture probe
QI	GAGTGTCCCGCGGCCCAGGA	Removes non-target-bound query probe

Table S3: The free energy (ΔG) and melting temperature (T_m) of query-target (Q-T) and query-competitor (Q-C) duplexes in different iSiMREPS sensors used for detection of miR-141.

Sensor ID	Complementary (bp)		ΔG (kcal/mol)		T_m (°C)	
	Q-T	Q-C	Q-T	Q-C	Q-T	Q-C
$Q_8C_6QS_{18}CS_3$	8	6	-13.56	-9.67	30.2	7.5
$Q_8C_6QS_{33}CS_3$	8	6	-13.56	-9.67	30.2	7.5
$Q_8C_7QS_{18}CS_3$	8	7	-13.56	-11.62	30.2	18.1
$Q_8C_7QS_{33}CS_3$	8	7	-13.56	-11.62	30.2	18.1

Note: ΔG and T_m were calculated using IDT oligo analyzer (https://www.idtdna.com/calc/analyzer) using the complementary segments that form the duplex.   All calculations were carried out at 25°C with 1µM oligo concentrations, 600 mM Na$^+$ ions.

Table S4: The free energy (ΔG) and melting temperature (T_m) of query-target (Q-T) and query-competitor (Q-C) duplexes for different iSiMREPS sensors used for detection of *EGFR* exon 19 deletion mutant DNA (*EGFR*Δexon_19).

Sensor ID	Complementary (bp)		ΔG (kcal/mol)		T_m (°C)	
	Q-T	Q-C	Q-T	Q-C	Q-T	Q-C
$Q_8C_6QS_{18}CS_4$	8	6	-11.7	-9.1	23.9	0
$Q_8C_6QS_{18}CS_{12}$	8	6	-11.7	-9.1	23.9	0
$Q_8C_6QS_{18}CS_{19}$	8	6	-11.7	-9.1	23.9	0
$Q_8C_7QS_{18}CS_4$	8	7	-11.7	-10.6	23.9	11.7
$Q_8C_8QS_{18}CS_4$	8	8	-11.7	-11.7	23.9	23.9

Note: ΔG was predicted using NUPACK(Caltech: , 2007; Zadeh et al., 2011) and T_m was calculated using IDT oligo analyzer (https://www.idtdna.com/calc/analyzer). The single stranded regions (spacers) flanking the complementary segments of query, target and competitor probe were considered to calculate ΔG using NUPACK(Caltech: , 2007; Zadeh et al., 2011), but only complementary segments were considered to calculate T_m using IDT oligo analyzer.   All calculations were carried out at 25°C with 1µM oligo concentrations, 600 mM Na$^+$ ions.

Table S5. The criteria for manually selecting traces from prism-based TIRF experiments.

Criterion	Rationale
Trace must have acceptor signal	Prevents traces with a bleached acceptor or no query probe from being included
Trace must not have multistep transitions	This convolutes the signal and makes it harder to separate genuine FRET transitions from off-target noise
Movies with signal that drifts into the baseline will not be accepted	Data from these movies is less trustworthy because of worsening S/N creating FRET states that can't be distinguished from noise
Unusually low High FRET or unusually high Low FRET values and S/N weak enough that it dips into baseline area	Traces with these features will be more susceptible to incorrect assignment of FRET states in HMM modeling
If there were multiple segments, the longest one was chosen and if they were of comparable lengths, the one with better S/N or clearer transitions was chosen.	This prevents the kinetic data from being too weighted or biased by a few traces with a large number of transitions.
If the final signal in a chosen segment is low FRET, it is only included if there is an acceptor signal after it.	This prevents signals after photobleaching of the acceptor from tainting the kinetic data
Traces with no distinction between baseline and signal are rejected	A static signal and an unusually intense baseline cannot be distinguished

Table S6. Acquisition parameters and default kinetic filtering criteria for different iSiMREPS sensors, with and without formamide, for detecting miR-141.

Parameter	Default	0%F 10s	0%F 30s	5%F	10%F	15%F	20%F
Frames	1-166	1-166	1-500	1-166	1-166	1-166	1-166
Exposure Time (s)	0.06	0.06	0.06	0.06	0.06	0.06	0.06
Intensity Threshold	200	200	200	200	200	200	200
Max Intensity	Inf	Inf	Inf	Inf	Inf	Inf	Inf
S/N Event Threshold	2	2	2	2	2	2	2
S/N Trace Threshold	3.5	4.5	3.8	4.5	3.4	3.4	1.4
Minimum N_{b+d}	5	2	4	4	3	5	6
Maximum N_{b+d}	Inf	Inf	Inf	Inf	Inf	Inf	Inf
Minimum $\tau_{on, median}$ (s)	0.06	0.24	0.18	0.06	0.06	0.06	0.06
Maximum $\tau_{on, median}$ (s)	10	9.9	19.98	7.38	7.44	1.38	2.7
Minimum $\tau_{off, median}$ (s)	0.06	0.12	0.18	0.06	0.06	0.06	0.06
Maximum $\tau_{off, median}$ (s)	0.9	3.3	6.06	2.82	2.1	1.2	0.6
Maximum $\tau_{on, event}$ (s)	5	Inf	22.5	8.82	3.96	9.78	9.54
Maximum $\tau_{off, event}$ (s)	4	Inf	15	5	4	4	2.34
Minimum τ_{on}, CV	Inf	Inf	Inf	Inf	Inf	Inf	Inf
Maximum τ_{on}, CV	Inf	Inf	Inf	Inf	Inf	Inf	Inf

Note: All experiments other than the ones indicated specifically in this table use the settings listed under "default". The formamide variance filtering settings shown here represent data from 1 trial and were obtained using the SiMREPS kinetic parameters optimizer, which gives a starting point of filtering settings to maximize counts and minimize false positives using real and control data sets. The exact filtering settings vary from day to day for formamide experiments, as they were selected using the optimizer to gauge each condition's best possible performance. The τ_{on} and τ_{off} indicate target bound (high-FRET) and non-target-bound (low-FRET) states, respectively.

Table S7. Acquisition parameters and default kinetic filtering criteria for different iSiMREPS sensors with and without formamide for detecting *EGFR* exon 19 deletion mutant DNA (*EGFR*Δ$_{exon\_19}$).

| Sensors	Q_8C_6 $QS_{18}CS_4$	Q_8C_6 $QS_{18}CS_{12}$	Q_8C_6 $QS_{18}CS_{19}$	Q_8C_7 $QS_{18}CS_{19}$	Q_8C_8 $QS_{18}CS_{19}$	Q_8C_6 $QS_{18}CS_{19}$	Q_8C_6 $QS_{18}CS_{19}$	Q_8C_6 $QS_{18}CS_{19}$
Formamide (%)	0	0	0	0	0	0	5-10	15-20
Start-to-end frame	1-200	1-200	1-200	1-200	1-200	1-100	1-100	1-100
Exposure time per frame (s)	0.1	0.1	0.1	0.1	0.1	0.1	0.1	0.1
Acquisition time (s)	20	20	20	20	20	10	10	10
Intensity threshold per trace	500	500	500	500	500	500	500	500
S/N threshold per event	1.5	1.5	1.5	1.5	1.5	1.5	1.5	1.5
S/N threshold per trace	1.7	3.7	2.6	2.9	4.5	1.5	1.5	1.5
Minimum N_{b+d}	5	5	5	5	5	5	6	8
Maximum N_{b+d}	Inf	Inf	Inf	Inf	Inf	Inf	Inf	Inf
Minimum $\tau_{on, median}$ (s)	0.1	0.3	0.1	0.1	0.1	0.1	0.1	0.1
Maximum $\tau_{on, median}$ (s)	10	10	10	10	10	6	6	6
Minimum $\tau_{off, median}$ (s)	0.1	0.1	0.1	0.1	0.1	0.1	0.1	0.1
Maximum $\tau_{off, median}$ (s)	10	10	10	10	10	6	6	6
Minimum τ_{on}, CV	Inf	Inf	Inf	Inf	Inf	Inf	Inf	Inf
Maximum τ_{on}, CV	Inf	Inf	Inf	Inf	Inf	Inf	Inf	Inf
Maximum $\tau_{on, event}$ (s)	12	12	12	12	12	8	8	8
Maximum $\tau_{off, event}$ (s)	12	12	12	12	12	8	8	8
Maximum $I_{low FRET state}$ per trace	Inf	Inf	Inf	Inf	Inf	Inf	Inf	Inf
Number of intensity states	2	2	2	2	2	2	2	2
Ignore post photobleaching (s)	12	12	12	12	12	8	8	8

Note: The default kinetic filtering criteria was determined by our newly developed machine learning based SiMREPS optimizer, which used data sets with multiple FOVs (e.g.., ≥ 10) from at least three independent experiments with and without the target as training data.   For each individual experiment, the default kinetic filtering criteria were optimized slightly to minimize false positives in the negative control without rejecting true positive counts in the positive sample. The τ_{on} and τ_{off} indicate target bound (high-FRET) and non-target-bound (low-FRET) states, respectively.

14

Table S8: Calculation of specificity for detecting *EGFR* exon 19 deletion mutant DNA (*EGFR*Δexon_19).

Mutant allele (%)	MUT (fM)	WT (nM)	C_{WT}/C_{MUT}	Counts ± s.d. in MUT +WT (n = 4)	Counts ± s.d. in WT-only (n = 4)	Specificity (%) = $[1 - \frac{FP}{TP \times (C_{WT}/C_{MUT})}] \times 100$
0.001	500	50	10^5	4.0 ± 1.2	1.2 ± 0.3	99.9996
0.0001	500	500	10^6	3.9 ± 0.7	1.3 ± 0.3	99.9999

3. Supplementary Figures
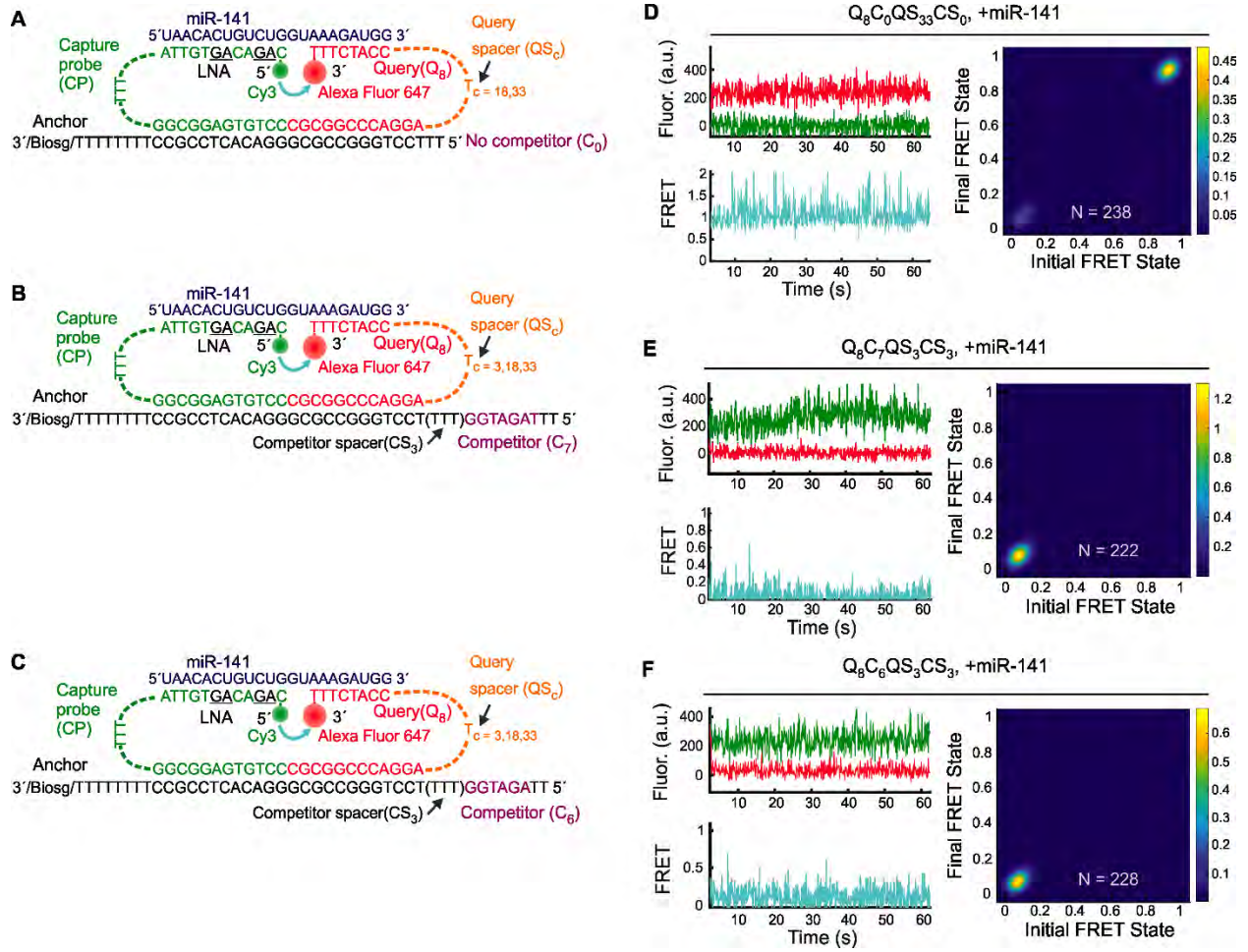
Fig. S1. Design and optimization of iSiMREPS sensors for detection of miR-141. (**A**) iSiMREPS sensor designs without any competitor sequence that differ only in the length of query spacer (i.e., 18 and 33 nt). (**B**) Sensor designs that contain a 7-nt competitor sequence that can interact with the query probe and vary in query spacer length (i.e., 3, 18 and 33 nt). (**C**) These iSiMREPS sensors contain a 6-nt competitor sequence and differ in the spacer lengths in the query probe. (**D-F**) Single-molecule kinetic traces, FRET signal, and TODP plots for the sensor $Q_8C_0QS_{18}CS_0$ (**D**), $Q_8C_7QS_3CS_3$ (**E**), and $Q_8C_6QS_3CS_3$ (**F**). All experiments were performed using preassembled anchor, capture, query and miR141 target at ~100 pM concentration and imaged under prism-TIRF microscopy. N represents number of molecules.
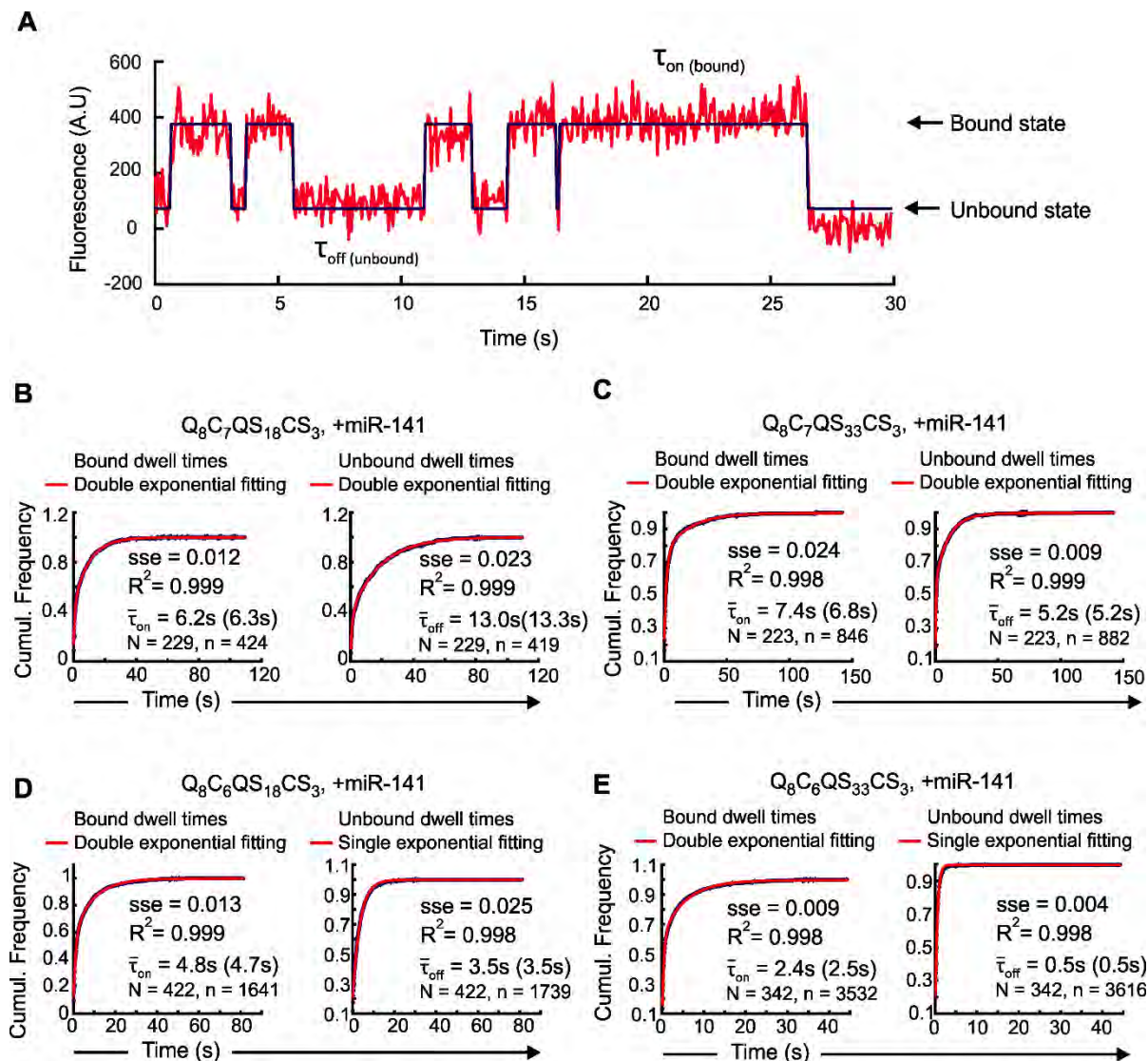
Fig. S2. Representative single molecule kinetic trace and estimation of average dwell times of FRET states for different iSiMREPS sensors for detecting miR-141. (**A**) Representative intensity-time trace fitted with tan HMM to extract the dwell times of miR-141 target bound ($\bar{\tau}_{on}$) and unbound states ($\bar{\tau}_{off}$). (**B-E**) Exponential fitting to dwell time cumulative frequency for miR-141 target bound (high-FERT) ($\bar{\tau}_{on}$) and non-target-bound (low-FRET) ($\bar{\tau}_{off}$) states for various sensors. All experiments were performed without formamide in the imaging buffer. Single exponential fitting was chosen when sum squared error (sse) <0.05 and R^2 > 0.98 and double exponential fitting was used otherwise. The time listed reflects the dwell time calculated from the best-fit curve using all accepted traces, and the time in parenthesis is the reported average when the data was split into 3 populations and is the one seen in the main text. The 'N' represents number of accepted traces, and 'n' represents the total number of dwell time events used for the fitting.

17
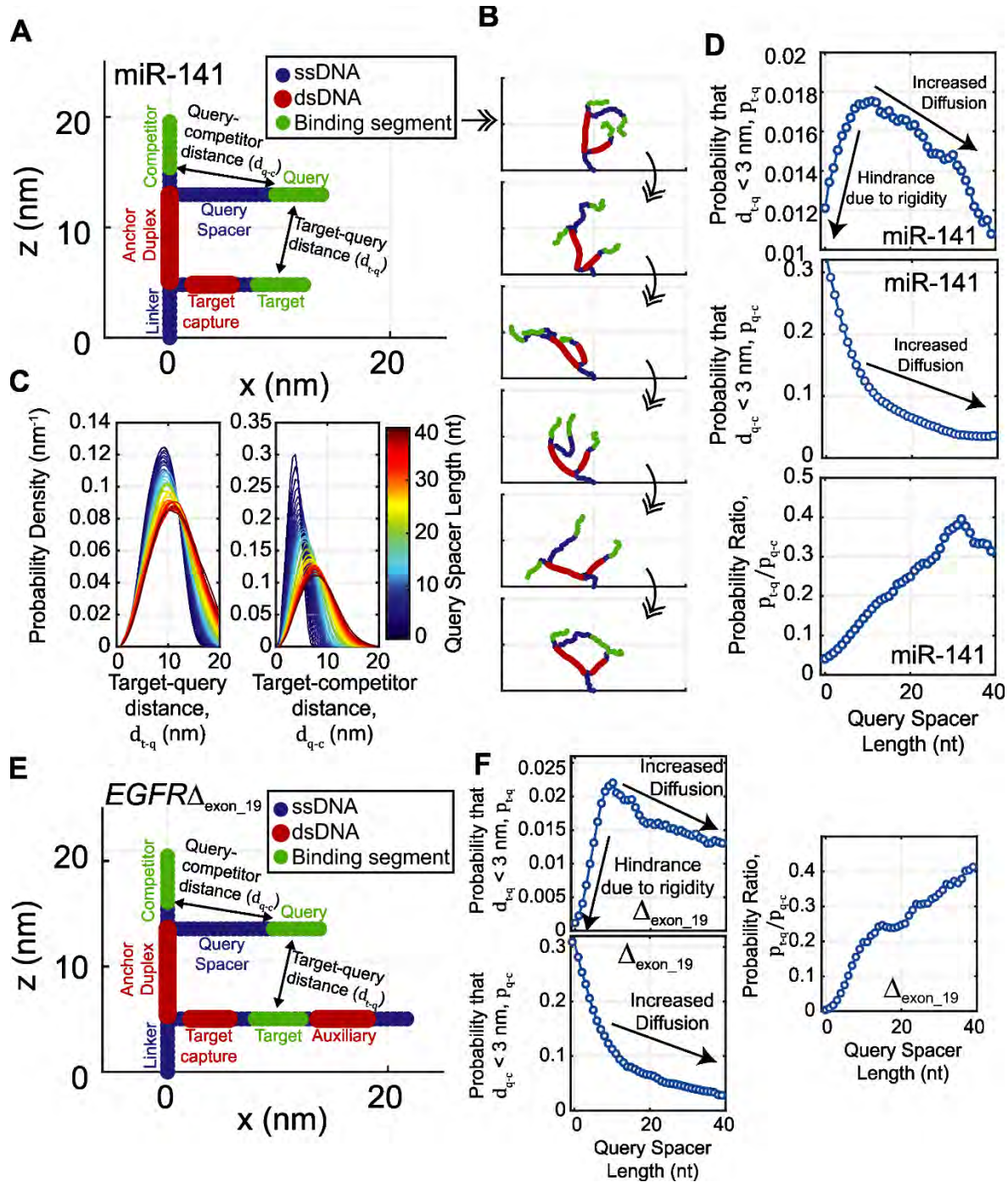
Fig. S3. Simulations support finding that iSiMREPS kinetics scale non-monotonically with query spacer length. (**A**) Initialized simulated iSiMREPS construct with labels showing the three main regions of the probe (anchor, query, and target) as well as the distances between the target and query segments (d_{t-q}) and the query and competitor segments (d_{q-c}) for the miR-141 construct. All points are represented as

circles with color denoted by polymer type as shown in the legend. (**B**) Six representative snapshots of a 2D version of the Monte Carlo simulation method, separated by at least 10,000 iterations each. (**C**) Probability density functions of d_{t-q} for simulations with query spacers lengths (depicted by color) ranging in length from 0 nt to 39 nt. (**D**) Three plots are shown. The top plot shows the probability (denoted p_{t-q}) that d_{t-q} is less than a close contact cutoff of 3 nm, as measured from the cumulative output of the Monte Carlo simulation, as a function of the query spacer length. The middle plot is similar, but for d_{q-c}. The bottom plot shows the ratio p_{t-q}/p_{q-c}. Because the activation energy for base pairing should be largely independent of spacer length and is also expected to be the rate-limiting step due to the high rate of diffusion, the strand association rate should scale linearly with p_{t-q}. Arrows in the top plot show that there are two roughly linear trend regimes. At query spacer lengths shorter than 9 nt, decreasing the spacer length decreases p_{t-q} by what we expect is a hindrance imposed by the long, stiff anchor duplex. In this regime, it is expected that this hindrance will also increase the rate of unbinding. In contrast, p_{q-c} decreases monotonically with increasing spacer length. This finding is consistent with the conformational rigidity model, as there are no dsDNA regions separating the competitor and query segments. At spacer lengths exceeding ~10 nt, increasing the spacer length mildly decreases p_{t-q} due to what we expect is an increased radius of diffusion. This trend is seen for p_{q-c} across the entire range of spacer lengths tested. However, while both p_{t-q} and p_{q-c} decrease monotonically with long spacer lengths, the ratio p_{t-q}/p_{q-c} increases monotonically across the entire range, suggesting that increasing spacer length monotonically increases the preference for the target's association with the target over the competitor. These findings hold true for cutoffs that are reasonably larger or smaller than 3 nm (not shown). Notably, this simulation method is limited in that it does not account for long-range repulsive interactions between non-neighboring regions of the probe. We expect that if we did incorporate such long-range interactions, different branches of the iSiMREPS probe would be further repelled by each other, potentially steepening the correlation observed in the long-spacer length regime. (**E**) Initialized simulated iSiMREPS *EGFR* exon 19 deletion mutant DNA (*EGFR*Δexon_19) construct with labels showing the three main regions of the probe (anchor, query, and target + auxiliary complex), like that shown in A. (**F**) Results for a simulation of the *EGFR*Δexon_19 design show similar trends to those shown in D.
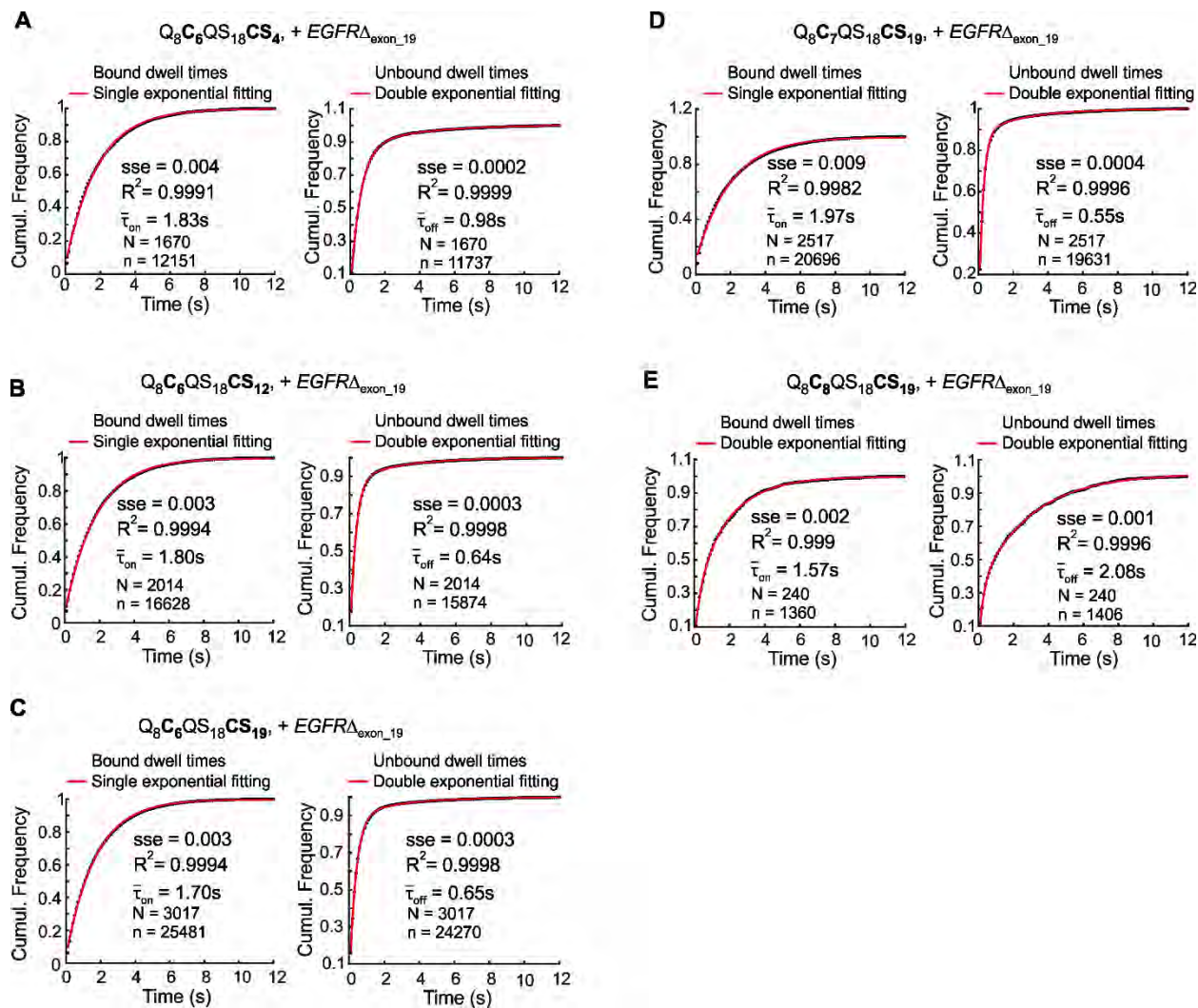
Fig. S4. Estimation of average dwell times smFRET states for different iSiMREPS sensors for detecting *EGFR* exon 19 deletion mutant DNA (*EGFR*Δexon_19). (**A-E**) Calculation of the average dwell time for the target bound (high-FRET) ($\overline{\tau}_{on}$) and non-target-bound (low-FRET) ($\overline{\tau}_{off}$) states for different iSiMREPS sensors for detecting *EGFR*Δexon_19. All experiments were performed without formamide in the imaging buffer. For all the sensors except the one with an 8-nt competitor, the target bound state dwell times were fitted with a single exponential. Single exponential fitting was chosen when sum squared error (sse) <0.08 and R^2 > 0.96, and double exponentials were used otherwise. All non-target-bound dwell times were fitted with a double exponential. All data is from 1 of 3 independent experiments. The 'N' represents number of accepted traces, and 'n' represents the total number of dwell time events used for the fitting.
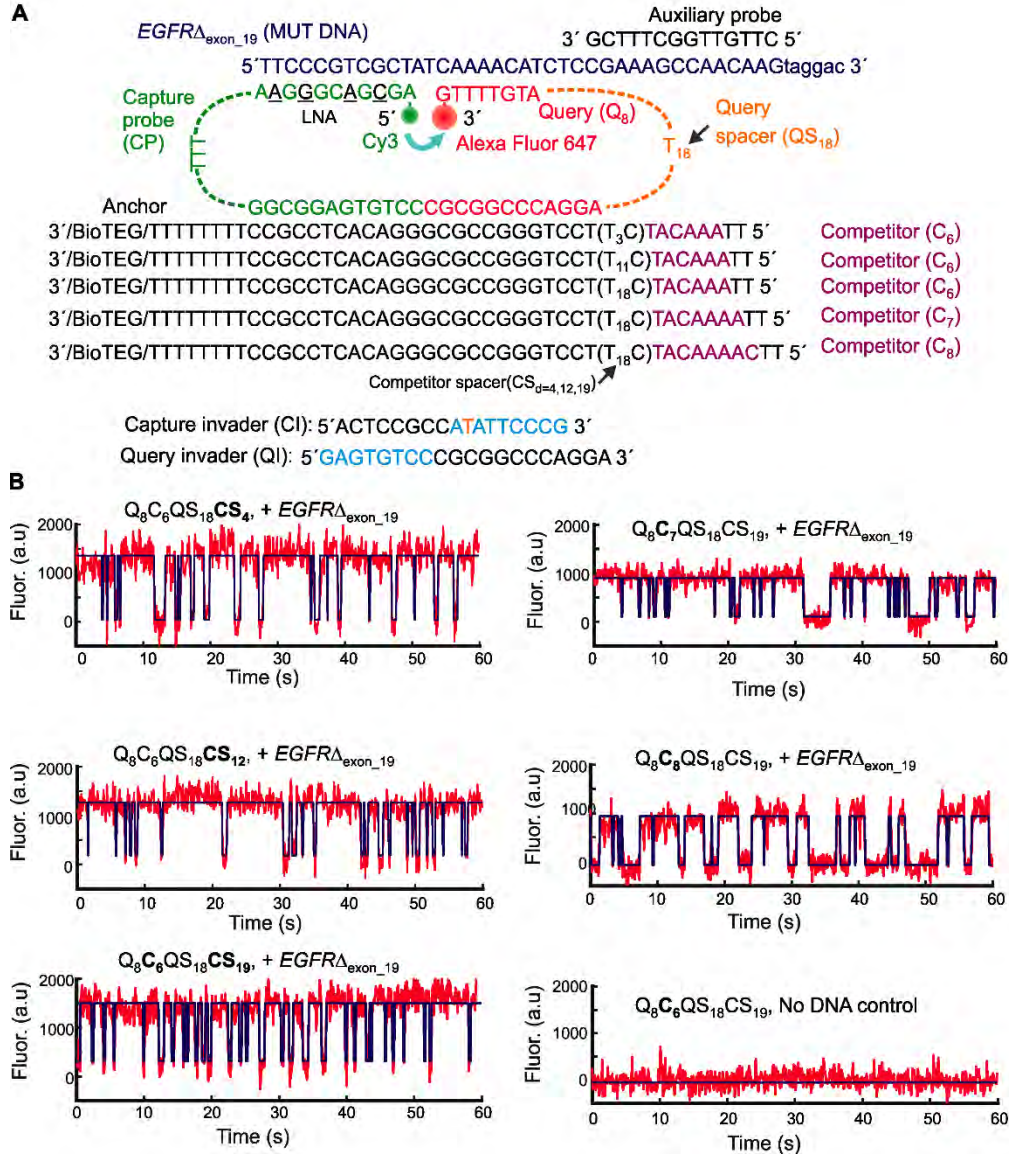
Fig. S5. Schematic of different iSiMREPS sensors and representative single molecule kinetic traces in the presence of *EGFR* exon 19 deletion mutant DNA (*EGFR*Δexon_19). (**A**) Designs of iSiMREPS sensors for detecting *EGFR*Δexon_19 with various competitor spacer (CS) and competitor (C) lengths. (**B**) Representative single-molecule kinetic traces (red) for different iSiMREPS sensors with or without *EGFR*Δexon_19 with an idealized hidden Markov model (HMM) fit (blue). All experiments were performed using 10 nM preassembled sensors consisting of anchor, capture and query probes, and 10 pM *EGFR*Δexon_19 forward strand. Imaging was done in 4x PBS (pH 7.4) at room temperature under an objective-type-TIRF microscope. The donor fluorophore (Cy3) was excited at 532 nm and the acceptor fluorescence (Alexa Fluor 647) was recorded as FRET signal.
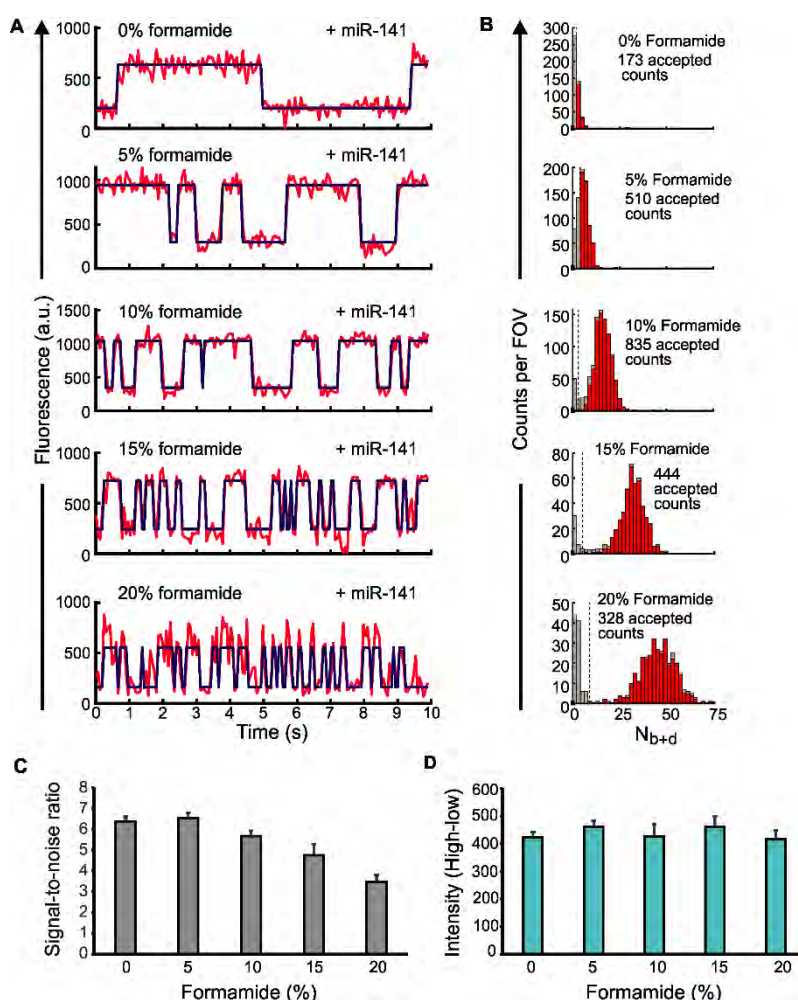
Fig. S6. Effects of formamide on the iSiMREPS sensor for detecting miR-141. (**A**) Representative traces for the $Q_8C_6QS_{18}CS_3$ miR-141 sensor at 0, 5, 10, 15, and 20% v/v formamide. The signal is in red while the idealized trace obtained from hidden Markov model (HMM) fitting is in blue. (**B**) Histograms from 1 of 3 independent experiments for each formamide condition that show the distribution of N_{b+d} among the accepted traces. These histograms reflect the distribution after application of filters for parameters such as signal-to-noise, intensity, and min and max average lifetimes. The red bars represent traces accepted while the grey bars represent traces rejected. (**C**) The average intensity difference between the high and low FRET states in the idealized hidden Markov model for each formamide condition. (**D**) The average signal-to-noise for a trace for each formamide condition. For all experiments shown, sensors were assembled at 200 nM in the presence of 5 nM miR-141. The pre-assembled sensors were then diluted it 1,000-fold and added to the surface. Imaging was performed in 4× PBS at pH 7.4. All data are presented as mean ± s.d. of 3 independent experiments.
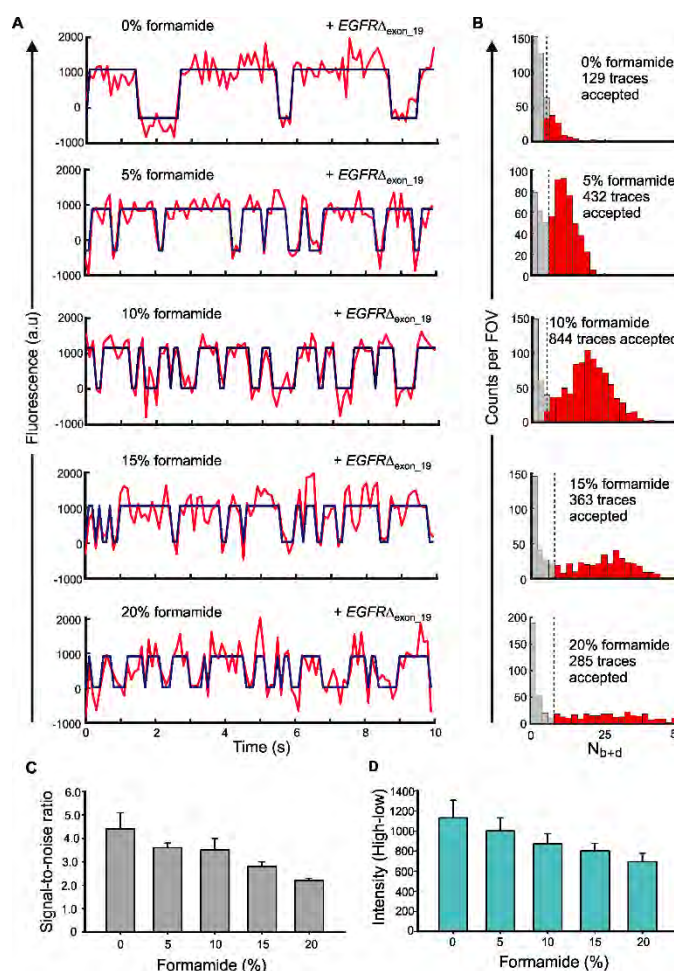
Fig. S7. Effects of formamide on the iSiMREPS sensor for detecting *EGFR* exon 19 deletion mutant DNA (*EGFR*Δ$_{exon\_19}$). (**A**) Representative single-molecule kinetic traces (red) with an idealized hidden Markov model (HMM) fit (blue) of the $Q_8C_6QS_{18}CS_{19}$ sensor for detecting *EGFR*Δ$_{exon\_19}$ at different formamide conditions. (**B**) Histograms of the number of candidate molecules per field-of-view (FOV) showing a given number of binding and dissociation events (N_{b+d}) after applying thresholds for FRET intensity, signal-to-noise, and dwell times of target-bound and non-target-bound states for each formamide condition. Red bars represent accepted traces while grey bars represent rejected traces. (**C, D**) The average signal-to-noise ratio (**C**), and difference in intensity of high- and low-FRET states (**D**) of the accepted traces for each formamide condition. All experiments were performed using 10 nM preassembled sensor consisting of anchor strand, capture and query probes, and 10 pM forward strands of *EGFR*Δ$_{exon\_19}$. Imaging was performed in 4x PBS (pH 7.4) at ambient room temperature under an objective-TIRF microscope. All data are presented as mean ± s.d. of 3 independent experiments.
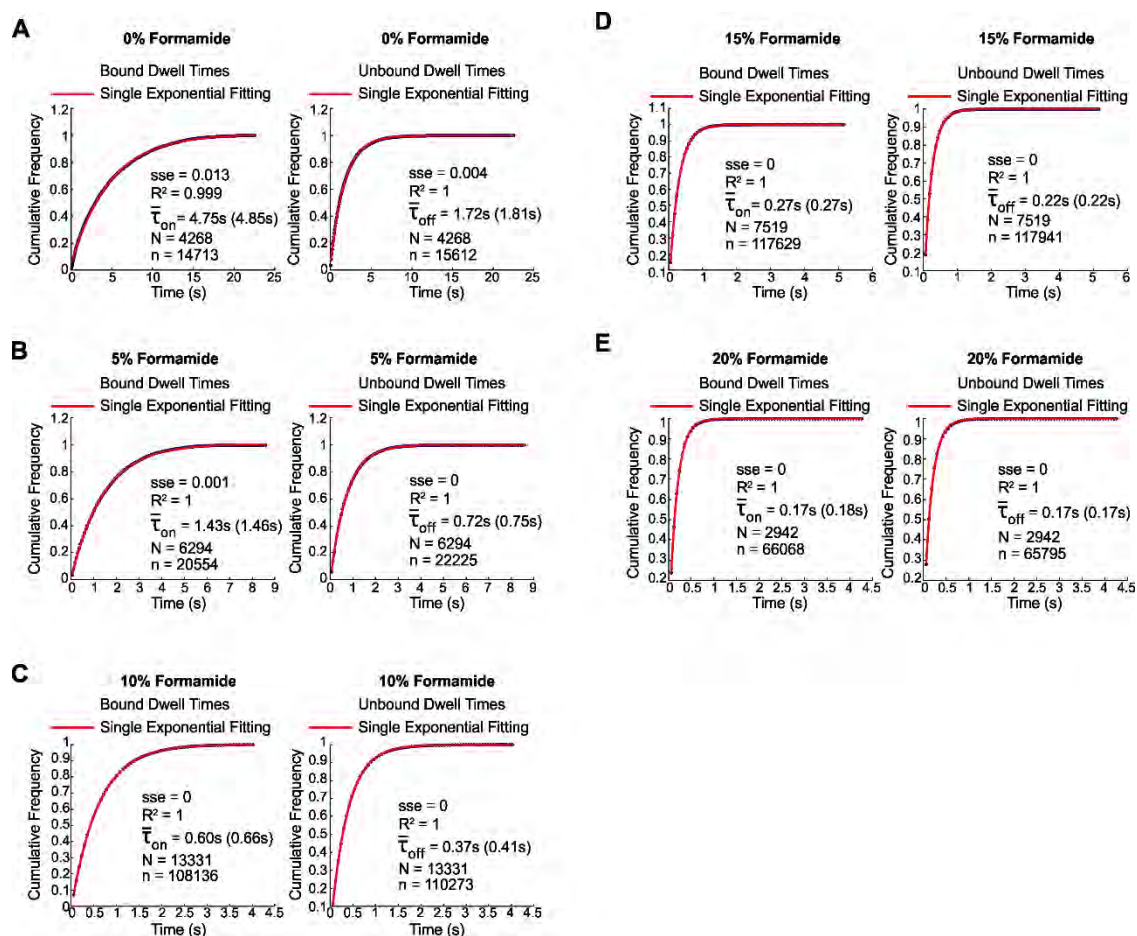
Fig. S8. Estimation of average dwell times of FRET states with the variation of formamide concentration using optimized iSiMREPS sensor for detecting miR-141. (**A-E**) Calculation of the average dwell time of high-($\overline{\tau}_{on}$) and low-FRET ($\overline{\tau}_{off}$) states for miR-141 for each formamide condition, obtained by fitting an exponential decay function to the cumulative frequency. Single exponential fits were used for all experiments depicted here as all had a sum squared error (sse) <0.05 and R^2 > 0.98. These curves represent the dwell times obtained in 1 of the 3 independent experiments conducted for each condition and the time in parentheses is the average time obtained from these independent experiments. The 'N' represents number of accepted traces, and 'n' represents the total number of apparent dwell time events in the accepted traces that used for the fitting. Experiments without formamide used a 30 s window to ensure accurate dwell times were obtained while a 10 s window was sufficient for all other conditions. The N value listed is the number of bound and unbound events in the accepted traces that contributed to the fitting.
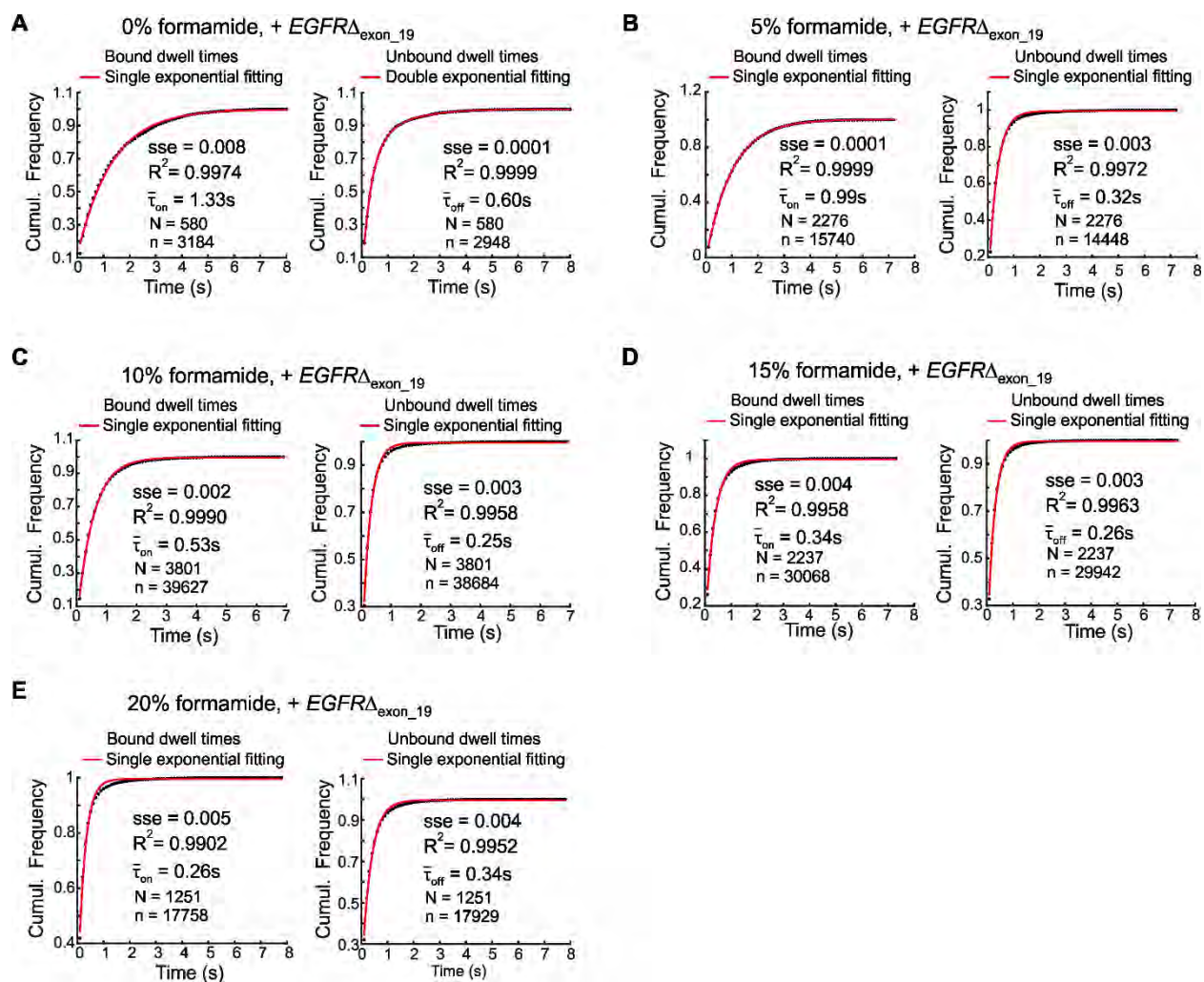
Fig. S9. Estimation of average dwell times of FRET states with the variation of formamide concentration using optimized iSiMREPS sensor for detecting *EGFR* exon 19 deletion mutant DNA (*EGFR*Δexon_19). **(A-E)** Calculation of the average dwell time for the target bound (high-FRET) ($\overline{\tau}_{on}$) and non-target-bound (low-FRET) ($\overline{\tau}_{off}$) states of the sensor $Q_8C_6QS_{18}CS_{19}$ for detecting *EGFR*Δexon_19 at different formamide concentrations (0-20% v/v) by fitting an exponential decay function to the cumulative frequency. Both target bound and non-target-bound dwell times for all conditions except 0% formamide were fitted with a single exponential decay function. Single exponential fitting was chosen when sum squared error (sse) <0.08 and R^2 > 0.96 and double exponential was used otherwise. All data are from 1 of 3 independent experiments. The 'N' represents number of accepted traces, and 'n' represents the total number of apparent dwell time events in the accepted traces that used for the fitting.
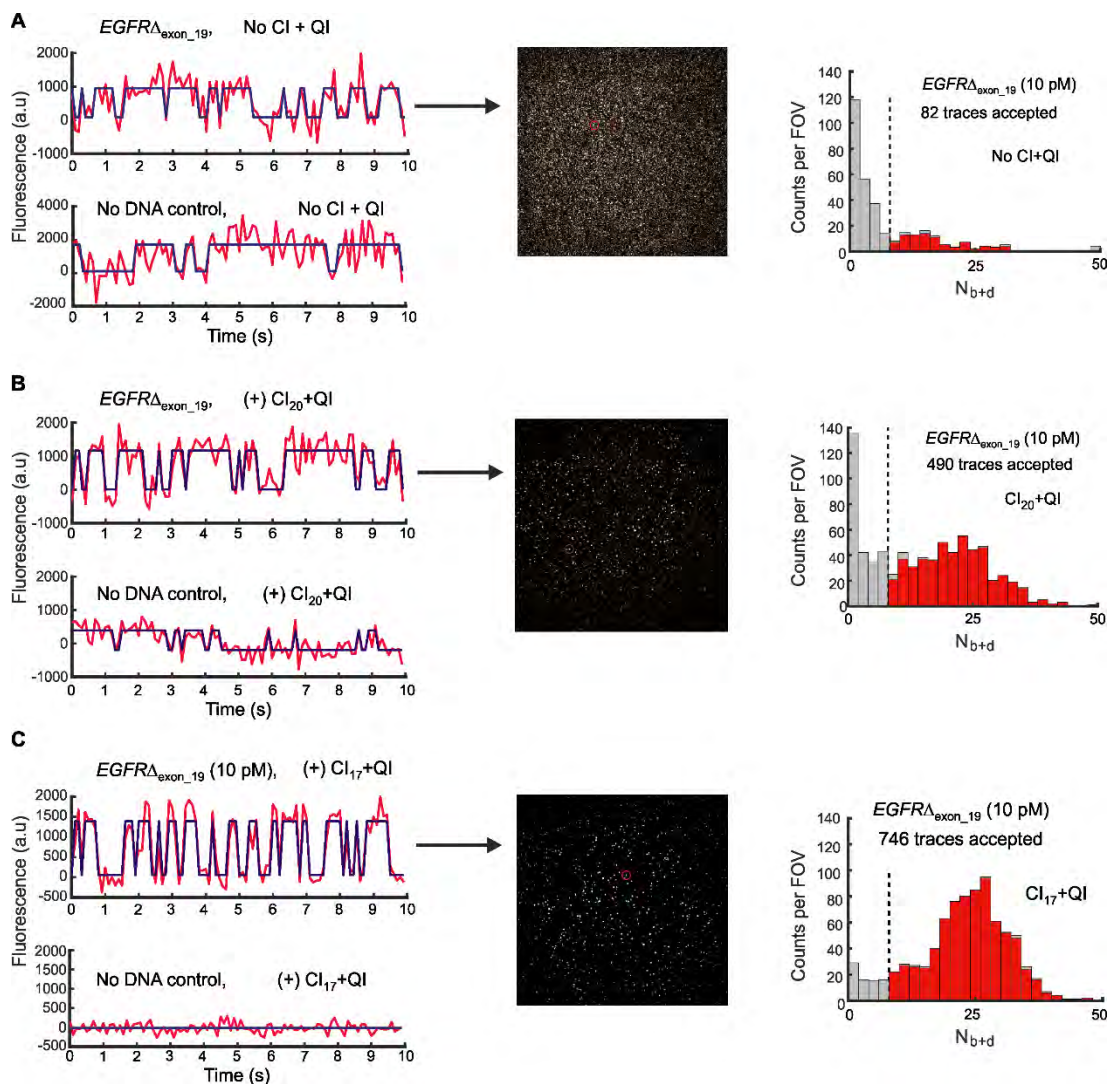
Fig. S10. Effect of different invaders on the background signals to detect *EGFR* exon 19 deletion mutant DNA (*EGFR*Δ exon_19). (**A-C**) Representative single-molecule kinetic traces, images of a field-of-view (FOV) and histograms of the number of candidate molecules per FOV showing a given number of binding and dissociation events (N_{b+d}) detected in 10 s per FOV, after applying thresholds for FRET intensity, S/N, and lifetimes of bound and unbound states without invaders (**A**), with invaders CI_{20}+QI (**B**), and with invaders CI_{17}+QI (**C**) in the presence and absence of *EGFR*Δ exon_19 target (see Figure 5A for invaders sequences). All experiments were performed using 0.2 mg/mL streptavidin (incubation: 10 min), 10 nM sensor (incubation: 30 min), 10 pM forward strands of *EGFR*Δ exon_19 (incubation: 90 min), 1 μM invaders (incubation: 20 min). Objective-TIRF imaging was performed in the presence of 10 % v/v formamide in the imaging buffer. All data are presented as the mean ± s.d. of n = independent experiments.
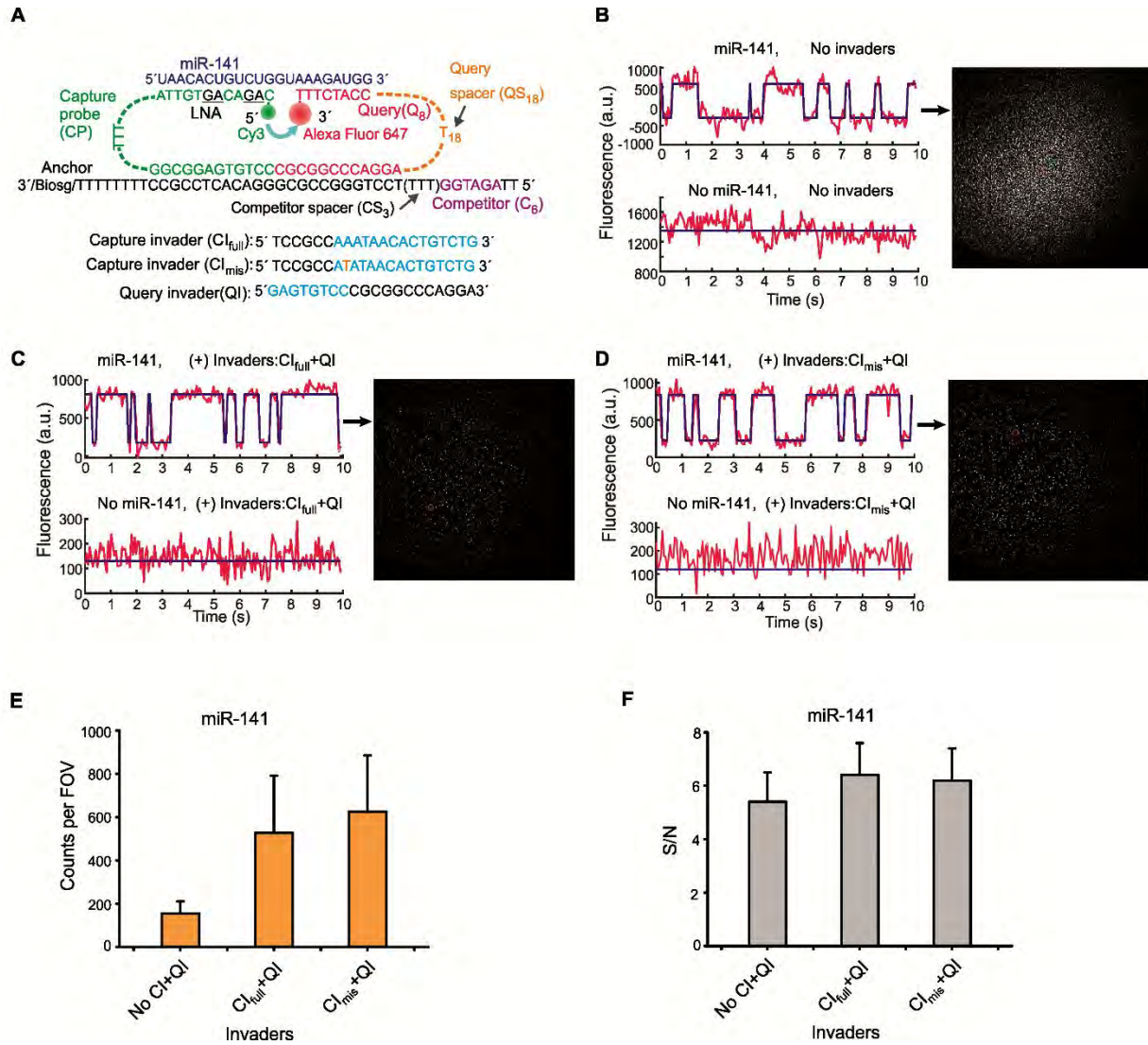
Fig. S11. Schematic of the design of iSiMREPS sensor for detecting miR-141 and representative single molecule kinetic traces in the presence and absence of different invaders. (**A**) Design of the optimized miR-141 sensor and different invaders tested. (**B-D**) Representative single-molecule kinetic traces and images of a FOV without invaders (**B**), with invaders CI_full+QI (**C**), and with invaders CI_mis+QI (**D**) in the presence and absence of miR-141. (**E**) Number of accepted counts per FOV in the presence of miR-141 after application of different capture invaders. (**F**) S/N ratio in the candidate target bound molecules after application of different capture invaders. Overall application of invaders improved the background signals as well the signal-to-noise ratio of single molecule traces as well as accepted counts compared to without invaders application. For all experiments shown, sensors were assembled at 200 nM in the presence of 5 nM miR-141. The pre-assembled sensors were then diluted it 1,000-fold and added to the surface. Imaging was performed in 4× PBS at pH 7.4. All data are presented as the mean ± s.d. of n = independent experiments.
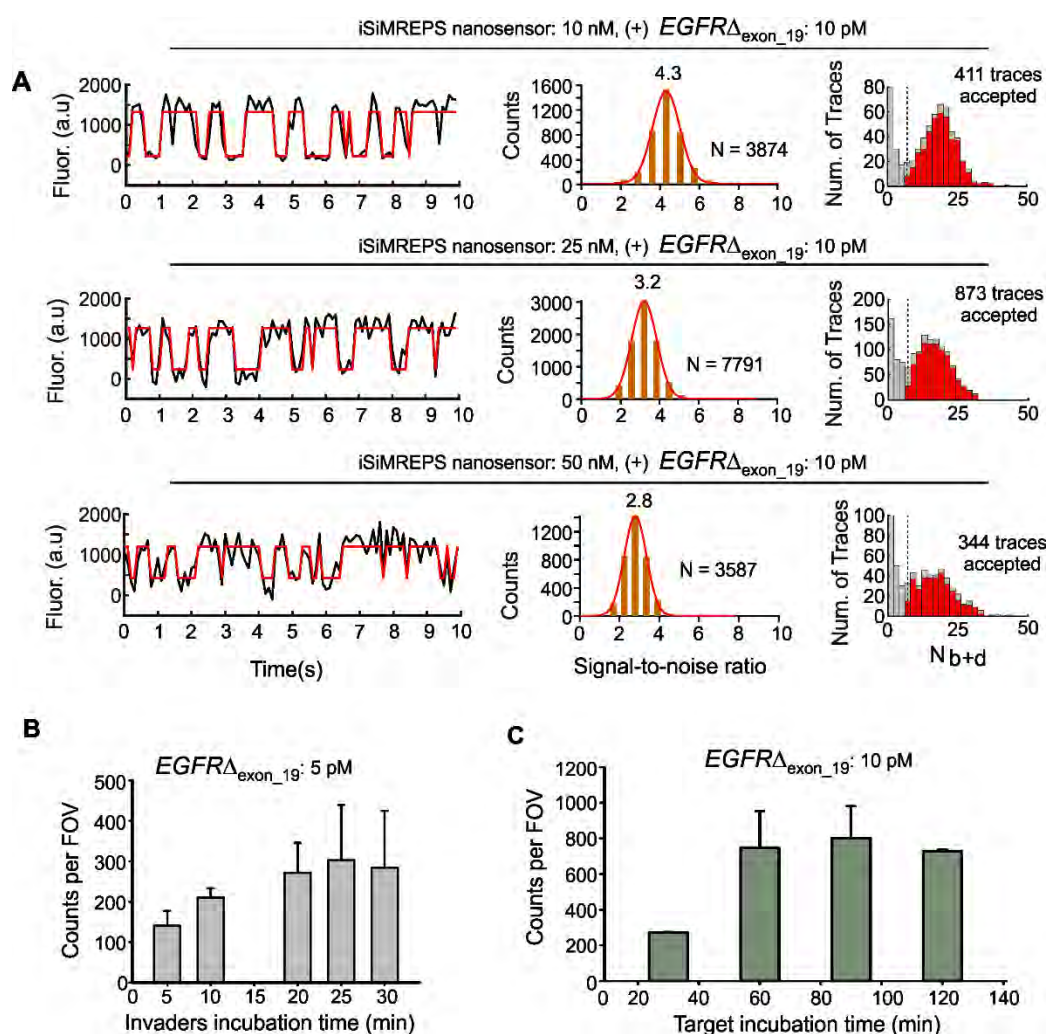
**Fig. S12.** Optimization of iSiMREPS assay conditions to enhance sensitivity for detection of *EGFR* exon 19 deletion mutant DNA (*EGFR*Δ_exon_19). (A) Effect of sensor concentration on signal-to-noise ratio (S/N) and the number of accepted traces. The experiment was performed using 10, 25, and 50 nM sensor (incubation: 30 min), 10 pM forward strands of *EGFR*Δ_exon_19 (incubation: 90 min), and 2.5 µM invaders (incubation: 20 min). (B) Effect of invaders incubation times on accepted traces. The experiment was performed using 25 nM sensor (incubation: 30 min), 5 pM forward strands of *EGFR*Δ_exon_19 (incubation: 90 min), and 2.5 µM invaders (incubation: 5, 10, 20, 25, 30 min). (C) Effect of target incubation times on accepted counts. This experiment was performed using 25 nM sensor (incubation: 30 min), 10 pM forward strands of *EGFR*Δ_exon_19 (incubation: 30, 60, 90, and 120 min), and 2.5 µM invaders (incubation: 25 min). All experiments were performed using the sensor $Q_8C_6QS_{18}CS_{19}$. All data are presented as mean ± s.d. of 2 independent experiments.

28
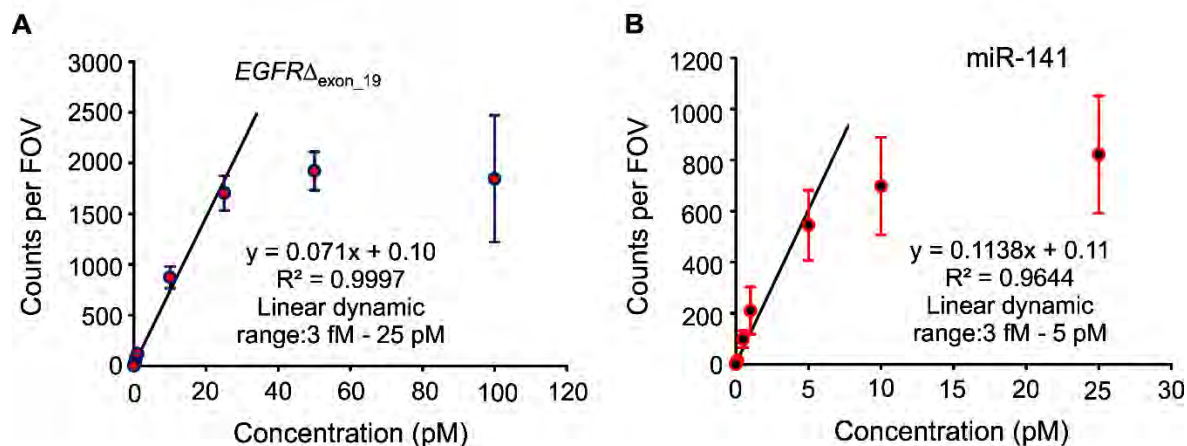
Fig. S13. Standard curves for miR-141 and *EGFR* exon 19 deletion mutant DNA (*EGFR*Δ_{exon_19}). (**A**) Standard curves showing the linear dynamic range for detection of *EGFR*Δ_{exon_19} dsDNA. The experiments were performed using a glass coverslip passivated with biotin-PEG: m-PEG at a 1:100 ratio, 0.5 mg/mL streptavidin incubation for 10 min, 25 nM sensor incubation for 30 min, 1.96 fM to 100 pM *EGFR*Δ_{exon_19}dsDNA incubation for 90 min, 2.5 µM invaders (CI$_{17}$ + QI) incubation for 20 min, and 10% v/v formamide. All data are presented as mean ± s.d., where n ≥ 3 independent experiments. iSiMREPS showed a linear dynamic range of approximately 3 fM - 25 pM for detecting *EGFR*Δ_{exon_19} which is approximately 3.9 orders of magnitude. (**B**) Standard curves showing linear dynamic range for detection of miR-141. The experiments were performed using a glass coverslip passivated with biotin-PEG: m-PEG at a ratio of 1:100, then incubated with 0.2 mg/mL streptavidin for 10 min, 10 nM sensor for 30 min, 2 fM to 50 pM miR-141 for 90 min, and 2 µM invaders (CI$_{mis}$ + QI) for 20 min. All imaging was performed with 10% v/v formamide. All data are presented as mean ± s.d. of ≥ 3 independent experiments. iSiMREPS showed a linear dynamic range of approximately 3 fM - 5 pM which is approximately 3.2 orders of magnitude.
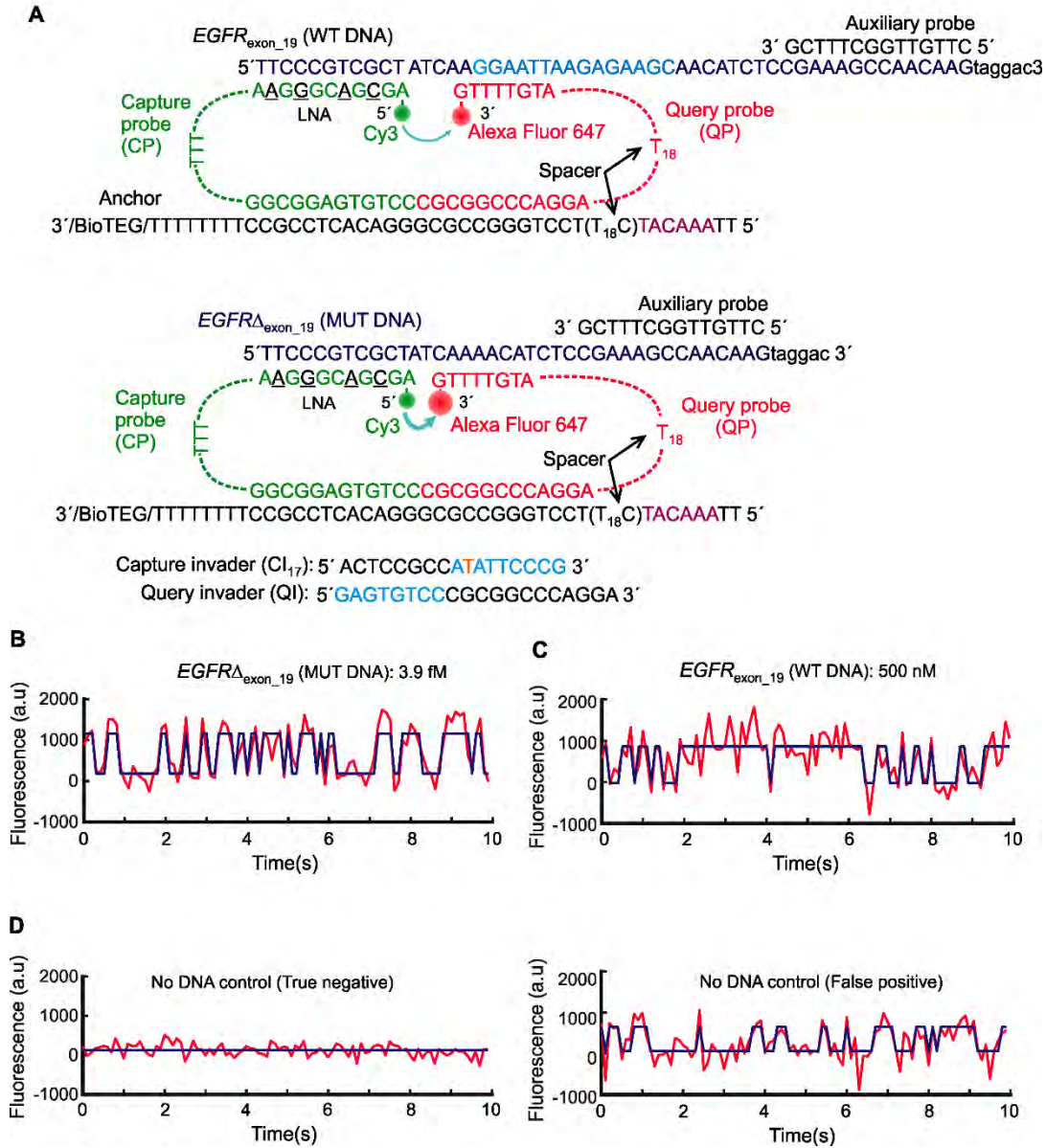
Fig. S14. Schematic of iSiMREPS sensor design for detecting *EGFR* exon 19 deletion mutant DNA (*EGFR*Δexon_19) and wild type DNA (*EGFR*exon_19) and representative single molecule kinetic traces. (**A**) Schematic of the iSiMREPS sensor for detection of *EGFR*Δexon_19and *EGFR*exon_19. The query probe was designed to be fully complementary to a short segment of the mutant DNA while lacking perfect complementarity with wild-type DNA.   Representative single molecule kinetic traces for *EGFR*Δexon_19at 3.9 fM (**B**) and *EGFR*exon_19 at 500 nM (**C**). (**D**) Representative true negative and false positive single molecule kinetic traces for no DNA target (control).
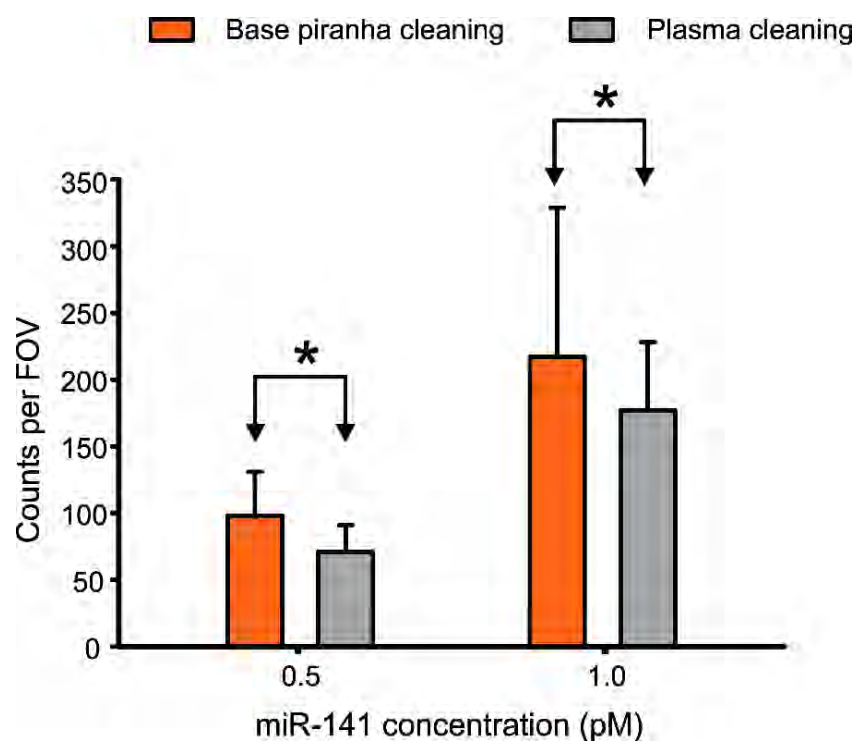
Fig. S15. Comparison of the performance of coverslip cleaning protocols for detecting miR-141. Base piranha cleaning protocol used a solution consisting of 14.3% v/v of 28-30 wt% NH_4OH, and 14.3% v/v of 30-35 wt% H_2O_2 that was heated to 70-80°C, whereas plasma cleaning protocol used application of plasma for 3 min to clean glass coverslip. The experiments were performed using a glass coverslip passivated with biotin-PEG: m-PEG at a ratio of 1:100, 10 nM sensor, 0.5 and 1.0 pM miR-141, and 2 µM invaders (CI_{mis} + QI). All imaging was performed with 10% v/v formamide. All data are presented as mean ± s.d. where n = 3 independent experiments. Single asterisk indicates the statistically insignificant differences at 95% confidence levels as assessed using a two-tailed, unpaired t test.

4 Supplementary References

Abelson, J., Blanco, M., Ditzler, M.A., Fuller, F., Aravamudhan, P., Wood, M., Villa, T., Ryan, D.E., Pleiss, J.A., Maeder, C., Guthrie, C., Walter, N.G., 2010. Nat. Struct. Mol. Biol. 17, 504-512.

Becker, N.B., Rosa, A., Everaers, R., 2010. E. Phys. J. E. 32, 53-69.

Blanco, M., Walter, N.G., 2010. Methods Enzymol. 472, 153-178.

Bronson, J.E., Fei, J., Hofman, J.M., Gonzalez, R.L., Jr., Wiggins, C.H., 2009. Biophys. J. 97, 3196-3205.

Caltech:, 2007.

Chatterjee, T., Li, Z., Khanna, K., Montoya, K., Tewari, M., Walter, N.G., Johnson-Buck, A., 2020. Trends Anal. Chem. 123, 115764.

Chen, H., Meisburger, S.P., Pabit, S.A., Sutton, J.L., Webb, W.W., Pollack, L., 2012. Proc. Natl. Acad. Sci. U. S. A. 109, 799.

Hayward, S.L., Lund, P.E., Kang, Q., Johnson-Buck, A., Tewari, M., Walter, N.G., 2018. J. Am. Chem. Soc. 140, 11755-11762.

Johnson-Buck, A., Li, J., Tewari, M., Walter, N.G., 2019. Methods 153, 3-12.

Marko, J.F., Siggia, E.D., 1995. Macromolecules 28, 8759-8770.

Saleh, O.A., McIntosh, D.B., Pincus, P., Ribeck, N., 2009. Phys. Rev. Lett. 102, 068301.

Seol, Y., Skinner, G.M., Visscher, K., 2004. Phys. Rev. Lett. 93, 118102.

Zadeh, J.N., Steenberg, C.D., Bois, J.S., Wolfe, B.R., Pierce, M.B., Khan, A.R., Dirks, R.M., Pierce, N.A., 2011. J. Comput. Chem. 32, 170-173.